PHYSICAL REVIEW D **83,** 025026 (2011)

Phase diagram of hot magnetized two-flavor color-superconducting quark matter

Sh. Fayazbakhsh* and N. Sadooghi†

Department of Physics, Sharif University of Technology, P.O. Box 11155-9161, Tehran, Iran

(Received 4 October 2010; published 31 January 2011)

A two-flavor color-superconducting Nambu–Jona-Lasinio model is introduced at finite temperature T, chemical potential μ, and in the presence of a constant magnetic field $\tilde{e}B$. The effect of $(T, \mu, \tilde{e}B)$ on the formation of chiral- and color-symmetry-breaking condensates is studied. The complete phase portrait of the model in $T-\mu$, $\mu-\tilde{e}B$, and $T-\tilde{e}B$ phase spaces for various fixed $\tilde{e}B$, T, and μ is explored. A threshold magnetic field $\tilde{e}B_t \simeq 0.5\ \mathrm{GeV}^2$ is found, above which the dynamics of the system are solely dominated by the lowest Landau level, and the effects of T and μ are partly compensated by $\tilde{e}B$.

DOI: 10.1103/PhysRevD.83.025026 PACS numbers: 12.38.−t, 11.30.Qc, 12.38.Aw, 12.39.−x

I. INTRODUCTION

Recently, the study of the properties of quark matter in the presence of strong uniform magnetic fields has attracted much attention. Possible effects caused by strong magnetic fields include magnetic catalysis [1,2], modification of the nature of electroweak phase transition [3], spontaneous creation of axial currents [4], formation of π_0 domain walls [5] and chiral density waves [6], chiral magnetic effect [7,8], and last but not least the influence on possible color-superconducting phases [9–16]. In this paper, we will focus on the magnetic catalysis and its possible effects on the phase diagram of a magnetized two-flavor color-superconducting (2SC) Nambu–Jona-Lasinio (NJL) model at finite temperature and chemical potential.[1] In particular, the dependence of the included meson and diquark masses on thermodynamic parameters, and possible interplay between these parameters on the formation of meson and diquark condensates and on the nature of phase transition, will be scrutinized.

At zero temperature, it is known that strong magnetic fields enhance the production of chiral and diquark condensates, albeit through different mechanisms, as it is described in [11]. Whereas magnetic catalysis of chiral symmetry breaking [1] is mainly responsible for dynamical mass generation and enhances the production of chiral condensates by increasing the particle-antiparticle interaction strength, a certain modification in the density of states of charged quarks near the Fermi surface, depending on the external magnetic field, reinforces the pairing of charged quarks and is made responsible for the enhancement of diquark production by a penetrating strong magnetic field [11]. In other words, in contrast to the effect of magnetic catalysis of chiral symmetry breaking, which is essentially based on a dimensional reduction of the dynamics of fermions from $D = 3 + 1$ to $D = 1 + 1$ dimensions to the regime of lowest Landau level (LLL) dominance [1], the pairing mechanism by color superconductivity, involving the charged quarks near the Fermi surface, is already $D = 1 + 1$-dimensional, and, therefore, the external magnetic field does not lead to any further dimensional reduction [11]. It is the goal of the present paper to explore the possible effects of finite T and μ on the above mechanisms of chiral and diquark production in the presence of strong magnetic fields. We will show that, in our setup, a certain threshold magnetic field exists, above which the dynamics of the system are solely dominated by the lowest Landau level, and the effects of T and μ are partly compensated by very large $\tilde{e}B$. The largest observed magnetic field in nature is $\sim 10^{12}$–10^{13} Gauß in pulsars and up to $\sim 10^{14}$–10^{15} Gauß on the surface of some magnetars, where the inner field is estimated to be of order $\sim 10^{18}$–10^{20} Gauß [22]. In the early Universe, magnetic fields of order $\sim 10^{47}$ Gauß may have been produced at the beginning of inflation [23]. Superconductive cosmic strings, if they exist, may have magnetic fields up to $\sim 10^{47}$–10^{48} Gauß in their vicinities [24]. In [25], it is shown that "the maximum value of magnetic field that delimits the range of values admitted without revising QED" is of order $\sim 10^{42}$ Gauß. There is also evidence for strong magnetic-field creation in noncentral heavy-ion experiments [26]. The early estimate of the magnetic field for the RHIC energy was made in [27], where it was shown that the magnitude of the magnetic field for an earlier stage of noncentral Au-Au collision at energy $\sqrt{s_{NN}} = 200$ GeV and impact parameter ~ 4 fm is about $eB \simeq 1.3 m_\pi^2 \simeq 0.025\ \mathrm{GeV}^2$, which corresponds to $B \simeq 4.3 \times 10^{18}$ Gauß.[2] Using a microscopic transport model, the authors in [28] estimate the lowest bound of the maximal magnetic-field strength at the LHC energy $\sqrt{s_{NN}} = 4.5$ TeV, with the same impact parameter, to be $eB \simeq 15 m_\pi^2 \simeq 0.3\ \mathrm{GeV}^2$, which is equivalent to $B \simeq 5 \times 10^{19}$ Gauß. Numerically, it is not *a priori* clear whether these amounts of magnetic fields are large enough to justify the LLL approximation,

---

*fayyazbaksh@physics.sharif.ir

†sadooghi@physics.sharif.ir

[1] Magnetic catalysis has various applications in cosmology [17], condensed matter physics [18], and particle physics [19–21].

[2] Here, $m_\pi = 140$ MeV. Moreover, $eB = 1\ \mathrm{GeV}^2$ corresponds to $B = 1.69 \times 10^{20}$ Gauß.

as it is done in [1] to demonstrate the magnetic catalysis of chiral symmetry breaking and in [11] to demonstrate the effect of strong magnetic fields on color superconductivity.

We have tried to answer this question, among others, in [16], where a color-neutral and dense 2SC-NJL model has been introduced in a (rotated) constant magnetic field at zero temperature. To do this, first the dependence of chiral- and color-symmetry-breaking condensates on the chemical potential μ and the rotated magnetic field $\tilde{e}B$ is determined analytically in a LLL approximation. Then, the meson and diquark masses are computed numerically for arbitrary magnetic fields. Comparing these analytical and numerical data, we have found a certain threshold magnetic field $\tilde{e}B_t \simeq 0.45$–$0.5\ \mathrm{GeV}^2$, corresponding to $B \simeq 8$–8.5×10^{19} Gauß, above which the system turns out to be dominated by LLL. Below $\tilde{e}B_t$, the chiral and diquark mass gaps oscillate with the external magnetic field. These oscillations are the results of the well-known van Alphen-de Haas effect [29], which occurs whenever Landau levels pass the quark Fermi surface. They are also observed in [21,30], where the dependence of chiral-symmetry-breaking mass gaps on constant magnetic fields is explored. Similar oscillations are also perceived in [14], where the diquark mass gap and the magnetization corresponding to the superconducting magnetized color-flavor locked (CFL) phase are determined as a function of external magnetic fields. For $\tilde{e}B > \tilde{e}B_t$, the system enters a "linear regime," where the mass gaps and the magnetization depend linearly on the external magnetic field. In this regime, where the system is believed to be solely affected by the dynamics of the fermions in the LLL, the numerical data coincide with the analytical results (see [16] for more detail). As concerns the phase diagram of the model introduced in [16], it is shown that a first-order phase transition occurs between the chiral symmetry breaking (χSB) and the color symmetry breaking (CSC) phases at $T = 0$ and $\mu \sim 350$–450 MeV. This transition is, then, followed by a second-order phase transition between the CSC phase into the normal quark matter.[3]

In the present paper, the same magnetized 2SC model will be considered at finite temperature. We are, in particular, interested in the additional effects of finite temperature, and will focus on the possible interplay between T, μ, and $\tilde{e}B$ on the formation of chiral- and color-symmetry-breaking condensates and on the nature of phase transitions. Our results may be relevant for the physics of heavy-ion collisions where, recently, the question of the accessibility of color-superconducting quark matter phases is pointed out [32]. The authors of [32] use a Polyakov-NJL model at finite temperature and density and present the corresponding QCD-phase diagram including, among others, mixed-phase regions of the first-order transition of 2SC-CFL quark matter and the second-order 2SC-normal phase transition. From this phase diagram, they conclude that the color-superconductor phase is already accessible at the present nuclotron-M energies $4 < E < 8$ AGeV, and that the possible transition from 2SC to normal quark matter becomes attainable in the planned FAIR-CBM and NICA-MPD experiments at $2 < E < 40$ AGeV. In this paper, the additional effect of constant magnetic fields that is believed to be created in noncentral heavy-ion collisions will be explored from a purely theoretical point of view. A complete phenomenological answer to the question of the accessibility of color-superconducting phases in heavy-ion collisions is out of the scope of this paper and will be postponed to future publications.

The organization of the paper is as follows: In Sec. II, we introduce our model for the hot magnetized two-flavor color-superconducting quark matter and determine the corresponding thermodynamic potential. In Sec. III, our numerical results on the dependence of the meson and diquark gaps on chemical potential, magnetic field, and temperature will be presented in Secs. III A 1–III A 3. In Sec. III B, the complete $T - \mu$, $T - \tilde{e}B$, and $\mu - \tilde{e}B$ phase portraits of the system at various fixed $\tilde{e}B$, μ, and T will be illustrated. The above-mentioned threshold magnetic field, $\tilde{e}B_t$, will be determined by comparing the analytical and the numerical results, corresponding to the second-order critical lines of the transition from the χSB and CSC phases to the normal phase, in a $T - \mu$ plane for $\tilde{e}B = 0.5, 0.7\ \mathrm{GeV}^2$ (Sec. III B 1) and in a $T - \tilde{e}B$ plane for $\mu = 0$ MeV (Sec. III B 2). The details of the analytical computations, which lead to second-order critical surfaces of these transitions in a $(T, \mu, \tilde{e}B)$ phase space, will be presented in the Appendix. Section IV is devoted to concluding remarks.

II. MAGNETIZED 2SC QUARK MATTER AT FINITE T AND μ

In Sec. II A, we briefly review our results from [16] and introduce a two-flavor NJL model, including the meson and diquark condensates at finite temperature and density and in the presence of a constant and uniform (rotated) magnetic field. In Sec. II B, the corresponding one-loop thermodynamic potential will be determined in a mean-field approximation.

A. The model

The Lagrangian density of a two-flavor gauged NJL model is given by

---

[3] As it is known from [31], in the regime of low temperature and large chemical potential, the 2SC phase goes over into the three-flavor CFL phase. In a two-flavor model, however, where no CFL phase can be built, only a simple transition from the 2SC to the normal phase is assumed to exist. The same assumption is also made in [16]. As we will note in Sec. III, our numerical results for low temperature and large chemical potential will be only of theoretical nature.

$$\begin{aligned}\mathcal{L}_f = {} & \bar{\psi}(x)[i\gamma^\mu(\partial_\mu - ieQA_\mu - igT^8G^8_\mu) + \mu\gamma^0]\psi(x) \\ & + G_S\{[\bar{\psi}(x)\psi(x)]^2 + [\bar{\psi}(x)i\gamma_5\vec{\tau}\psi(x)]^2\} \\ & + G_D\{[i\bar{\psi}^C(x)\varepsilon_f\epsilon_c^3\gamma_5\psi(x)][i\bar{\psi}(x)\varepsilon_f\epsilon_c^3\gamma_5\psi^C(x)]\}.\end{aligned} \tag{2.1}$$

Here, $\psi^C = C\bar{\psi}^T$ and $\bar{\psi}^C = \psi^T C$ are charge-conjugate spinors, $C = i\gamma^2\gamma^0$ is the conjugation matrix, and $\vec{\tau} = (\tau_1, \tau_2, \tau_3)$ are Pauli matrices. Moreover, $(\varepsilon_f)_{ij}$ and $(\epsilon_c^3)^{ab} \equiv (\epsilon_c)^{ab3}$ are antisymmetric matrices in color and flavor spaces, respectively. For a theory with two quark flavors and three color degrees of freedom, the flavor indices $i, j = (1, 2) = (u, d)$, and the color indices $a, b = (1, 2, 3) = (r, g, b)$. The quarks are taken to be massless $m_u = m_d = 0$. The quark chemical potential that is responsible for the nonzero baryonic density of quark matter is denoted by μ. Here, $T^8 = \frac{\lambda_8}{2}$, where $\lambda_8 = \frac{1}{\sqrt{3}}\,\mathrm{diag}(1, 1, -2)$, the 8th Gell-Mann λ matrix. The scalar and diquark couplings are denoted by G_S and G_D, respectively. The charge matrix $Q \equiv Q_f \otimes \mathbf{1}_c$, where $Q_f \equiv \mathrm{diag}(2/3, -1/3)$ is the fermionic charge matrix coupled to the $U(1)$ gauge field A_μ. The same setup, with an additional color-chemical potential μ_8 imposing the color neutrality of the theory, is also used in [16] to study the effect of a magnetic field on quark matter under extreme conditions. Following the same steps as in [16] to determine the Lagrangian density containing the chiral and diquark condensates in an appropriate Nambu-Gorkov form (NG), we define first the mesonic fields

$$\sigma = -2G_S(\bar{\psi}\psi) \quad \text{and} \quad \vec{\pi} = -2G_S(\bar{\psi}i\gamma^5\vec{\tau}\psi), \tag{2.2}$$

as well as the diquark fields

$$\begin{aligned}\Delta &= -2G_D(i\bar{\psi}^C\varepsilon_f\epsilon_c^3\gamma_5\psi) \quad \text{and} \\ \Delta^* &= -2G_D(i\bar{\psi}\varepsilon_f\epsilon_c^3\gamma_5\psi^C).\end{aligned} \tag{2.3}$$

Combining, then, the gauge fields A_μ and G^8_μ using the "rotated" charge operator $\tilde{Q} = Q_f \otimes 1_c - 1_f \otimes (\frac{\lambda_8}{2\sqrt{3}})_c$, the rotated massless $U_{em}(1)$ field $\tilde{A}_\mu = A_\mu\cos\theta - G^8_\mu\sin\theta$, as well as the massive in-medium 8th gluon field $\tilde{G}^8_\mu = A_\mu\sin\theta + G^8_\mu\cos\theta$, can be derived (see [16] for more details). Replacing $\tilde{A}_\mu$ with an external gauge field $\tilde{A}^{\text{ext}}_\mu = (0, 0, Bx, 0)$ in the Landau gauge, a constant rotated background $U(1)$ magnetic field directed in the third direction $\tilde{\mathbf{B}} = B\mathbf{e}_3$ is induced. Neglecting, then, the massive gauge boson $\tilde{G}^8_\mu$, the total modified bosonized Lagrangian density, $\tilde{\mathcal{L}} = \tilde{\mathcal{L}}_k + \tilde{\mathcal{L}}_f$, in the presence of a uniform magnetic field, arises. It consists of a kinetic term

$$\tilde{\mathcal{L}}_k \equiv -\left(\frac{\sigma^2}{4G_S} + \frac{|\Delta|^2}{4G_D} + \frac{B^2}{2}\right) \tag{2.4}$$

and an interaction term

$$\begin{aligned}\tilde{\mathcal{L}}_f = {} & \bar{\psi}(x)[i\gamma^\mu(\partial_\mu - i\tilde{e}\,\tilde{Q}\,\tilde{A}^{\text{ext}}_\mu) + \mu\gamma^0 - \sigma]\psi(x) \\ & - \tfrac{1}{2}\{\Delta^*[i\bar{\psi}^C(x)\varepsilon_f\epsilon_c^3\gamma_5\psi(x)] \\ & + \Delta[i\bar{\psi}(x)\varepsilon_f\epsilon_c^3\gamma_5\psi^C(x)]\}.\end{aligned} \tag{2.5}$$

Assuming that the vacuum of the system is characterized by $\langle\sigma\rangle \neq 0$ and $\langle\vec{\pi}\rangle = 0$, we have neglected the $\vec{\pi}$ mesons. Moreover, using the definition of the rotated charge operator $\tilde{Q}$ in a six-dimensional flavor-color representation $(u_r, u_g, u_b, d_r, d_g, d_b)$, the rotated $\tilde{q}$ charges of different quarks, in units of $\tilde{e} = e\cos\theta$, are given by

quarks	u_r	u_g	u_b	d_r	d_g	d_b
$\tilde{q}$	$+\frac{1}{2}$	$+\frac{1}{2}$	1	$-\frac{1}{2}$	$-\frac{1}{2}$	0

To bring the above Lagrangian density $\tilde{\mathcal{L}}_f$ in a more appropriate Nambu-Gorkov form, we introduce, at this stage, the rotated charge projectors $\Omega_{\tilde{q}}$,

$$\begin{aligned}\Omega_0 &= \mathrm{diag}(0, 0, 0, 0, 0, 1), \\ \Omega_1 &= \mathrm{diag}(0, 0, 1, 0, 0, 0), \\ \Omega_{+(1/2)} &= \mathrm{diag}(1, 1, 0, 0, 0, 0), \\ \Omega_{-(1/2)} &= \mathrm{diag}(0, 0, 0, 1, 1, 0),\end{aligned} \tag{2.6}$$

that satisfy $\tilde{Q}\Omega_{\tilde{q}} = \tilde{q}\Omega_{\tilde{q}}$. The Nambu-Gorkov bispinors are, then, defined by

$$\Psi_{\tilde{q}} = \begin{pmatrix}\psi_{\tilde{q}} \\ \psi^C_{-\tilde{q}}\end{pmatrix},$$

where $\psi_{\tilde{q}}(x) \equiv \Omega_{\tilde{q}}\psi(x)$. In terms of $\bar{\Psi}_{\tilde{q}}$ and $\Psi_{\tilde{q}}$, the Lagrangian density $\tilde{\mathcal{L}}_f$ from (2.5) in the Nambu-Gorkov form reads (for more details see [16]):

$$\tilde{\mathcal{L}}_f = \frac{1}{2}\sum_{\tilde{q}\in\{0,1,\pm(1/2)\}}\bar{\Psi}_{\tilde{q}}(x)\mathcal{S}_{\tilde{q}}\Psi_{\tilde{q}}(x). \tag{2.7}$$

For $\tilde{q} \in \{0, 1\}$, $\mathcal{S}_{\tilde{q}}$ is given by

$$\mathcal{S}_{\tilde{q}\in\{0,1\}} \equiv \begin{pmatrix}[G^+_{(\tilde{q})}]^{-1} & 0 \\ 0 & [G^-_{(\tilde{q})}]^{-1}\end{pmatrix}, \tag{2.8}$$

and for $\tilde{q} \in \{-\frac{1}{2}, +\frac{1}{2}\}$, it reads

$$\mathcal{S}_{\tilde{q}\in\{-(1/2),+(1/2)\}} \equiv \begin{pmatrix}[G^+_{(\tilde{q})}]^{-1} & -\kappa\Omega_{-\tilde{q}} \\ -\kappa'\Omega_{\tilde{q}} & [G^-_{(\tilde{q})}]^{-1}\end{pmatrix}. \tag{2.9}$$

Here,

$$[G^\pm_{(\tilde{q})}]^{-1} \equiv \gamma^\mu(i\partial_\mu + \tilde{e}\,\tilde{q}\,\tilde{A}_\mu - \sigma \pm \mu\delta_{\mu 0}), \tag{2.10}$$

and $\kappa^{ij,ab}_{\alpha\beta} \equiv i\Delta\tau_2^{ij}\lambda_2^{ab}\gamma^5_{\alpha\beta}$, as well as $\kappa' \equiv \gamma_0\kappa^\dagger\gamma_0 = i\Delta^*\tau_2\lambda_2\gamma^5$. In the next section, the Lagrangian density $\tilde{\mathcal{L}}$, with $\tilde{\mathcal{L}}_k$ in (2.4) and $\tilde{\mathcal{L}}_f$ in (2.7)–(2.10), will be used to determine the thermodynamic potential of this model in the mean-field approximation.

B. Thermodynamic potential

The quantum effective action of the theory, $\Gamma_{\rm eff}$, is defined by integrating out the fermionic degrees of freedom using the path integral

$$e^{i\Gamma_{\rm eff}[\sigma,\Delta,\Delta^*]}=\int\mathcal{D}\psi\mathcal{D}\bar{\psi}\exp\left(i\int d^4x\tilde{\mathcal{L}}\right). \tag{2.11}$$

At the one-loop level, it consists of two parts: the tree-level and the one-loop effective action, $\Gamma^{(0)}_{\rm eff}$ and $\Gamma^{(1)}_{\rm eff}$. In the mean-field approximation, where the order parameters $\sigma\equiv\langle\sigma(x)\rangle$, $\Delta\equiv\langle\Delta(x)\rangle$, and $\Delta^*\equiv\langle\Delta^*(x)\rangle$ are constant, the tree-level part of $\Gamma_{\rm eff}$ is given by

$$\Gamma^{(0)}_{\rm eff}[\sigma,\Delta,\Delta^*;B]=-\mathcal{V}\left(\frac{\sigma^2}{4G_S}+\frac{|\Delta|^2}{4G_D}+\frac{B^2}{2}\right). \tag{2.12}$$

Here, $\mathcal{V}$ is a four-dimensional space-time volume, and $|\Delta|^2=\Delta\Delta^*$. The one-loop effective action is given by

$$\Gamma^{(1)}_{\rm eff}[\sigma,\Delta,\Delta^*;B]=-\frac{i}{2}\sum_{\tilde{q}}{\rm Tr}_{{\rm NG}cfsx}\ln[\mathcal{S}^{-1}_{\tilde{q}}], \tag{2.13}$$

where $\mathcal{S}_{\tilde{q}}$ is defined in (2.8)–(2.10). In (2.13), the trace operation includes, apart from a two-dimensional trace in the NG space , a trace over color (c), flavor (f), and spinor (s) degrees of freedom, as well as a trace over a four-dimensional space-time coordinate (x). After performing the trace operation over the NG, c, f, and s using the method described in [16], we arrive at

$$\tilde{\Gamma}^{(1)}_{\rm eff}(\bar{p})=\sum_{\kappa\in\{r,g,b\}}\tilde{\Gamma}^{(1)/\kappa}_{\rm eff}(\bar{p}), \tag{2.14}$$

which includes the contribution of the blue (b), red (r), and green (g) quarks

$$\begin{aligned}\tilde{\Gamma}^{(1)/{\rm b}}_{\rm eff}(\bar{p})&=-i\sum_{\tilde{q}\in\{0,1\}}\ln\det{}_x[\{(E_{\tilde{q}}+\mu)^2-p_0^2\}\{(E_{\tilde{q}}-\mu)^2-p_0^2\}],\\ \sum_{c\in\{r,g\}}\tilde{\Gamma}^{(1)/c}_{\rm eff}(\bar{p})&=-2i\sum_{\tilde{q}\in\{+(1/2),-(1/2)\}}\ln\det{}_x[(E^{(+1)2}_{\tilde{q}}-p_0^2)(E^{(-1)2}_{\tilde{q}}-p_0^2)].\end{aligned} \tag{2.15}$$

Here, $\bar{p}$ is a modified four-momentum defined by [8]

$$\begin{aligned}\bar{p}^{\,\mu}_{\tilde{q}\neq0}&=\left(p_0,0,\frac{\tilde{q}}{|\tilde{q}|}\sqrt{2|\tilde{q}\,\tilde{e}\,B|n},p_3\right)\quad\text{for }\tilde{q}=1,\pm\frac{1}{2},\\ \bar{p}^{\mu}_{\tilde{q}=0}&=(p_0,\mathbf{p})\quad\text{for }\tilde{q}=0,\end{aligned} \tag{2.16}$$

with $\mathbf{p}\equiv(p_1,p_2,p_3)$. In (2.15), $E_{\tilde{q}}$ are given by the dispersion relations corresponding to the neutral and charged particles [16]

$$\begin{aligned}E_{\tilde{q}}&=\sqrt{2|\tilde{q}\,\tilde{e}\,B|n+p_3^2+\sigma^2}\quad\text{for }\tilde{q}=1,\pm\frac{1}{2},\\ E_0&=\sqrt{\mathbf{p}^2+\sigma^2}\quad\text{for }\tilde{q}=0.\end{aligned} \tag{2.17}$$

Moreover, we have $E^{(\pm1)}_{\tilde{q}}=\sqrt{(E_{\tilde{q}}\pm\mu)+|\Delta|^2}$. Performing the remaining determinant in the coordinate space, a space-time volume factor $\mathcal{V}$ arises. Combining, then, the resulting expression with the tree-level part of the effective action from (2.12), the effective action of the theory can be given in terms of the effective thermodynamic (mean-field) potential $\Omega_{\rm eff}$ as $\Gamma_{\rm eff}=-\mathcal{V}\Omega_{\rm eff}$. Introducing, now, discrete Matsubara frequencies by replacing p_0 with $p_0=i\omega_\ell$, where $\omega_\ell=\frac{\pi}{\beta}(2\ell+1)$, and $\beta\equiv T^{-1}$, the one-loop effective potential $\Omega^{(1)}_{\rm eff}\equiv-\frac{1}{V\beta}\tilde{\Gamma}^{(1)}_{\rm eff}$ is first given by[4]

$$\begin{aligned}\Omega^{(1)}_{\rm eff}(\tilde{e}B,T,\mu)&\\ =-\frac{1}{V\beta}\sum_{\mathbf{p}}\sum_{\ell=-\infty}^{\infty}\sum_{\kappa=\pm1}&\Bigg\{\sum_{\tilde{q}\in\{0,1\}}\ln[\omega_\ell^2+(E_{\tilde{q}}+\kappa\mu)^2]\\ &+2\sum_{\tilde{q}\in\{+(1/2),-(1/2)\}}\ln[\omega_\ell^2+E^{(\kappa)2}_{\tilde{q}}]\Bigg\}.\end{aligned} \tag{2.18}$$

Converting, then, the logarithms into proper-time integrals over the dimensionful variable s and using the Poisson resummation formula

$$\sum_{\ell=-\infty}^{\infty}e^{-s[(2\pi\ell/\beta)+x]^2}=\frac{\beta}{2\sqrt{\pi s}}\left[1+2\sum_{\ell=1}^{\infty}\cos(x\beta\ell)e^{-(\beta^2\ell^2/4s)}\right] \tag{2.19}$$

to separate the resulting expression into temperature-dependent and temperature-independent parts, we arrive at the one-loop effective potential of our model:

$$\begin{aligned}\Omega^{(1)}_{\rm eff}(\tilde{e}B,T,\mu)=\frac{1}{2\sqrt{\pi}V}\sum_{\mathbf{p}}\sum_{\kappa=\pm1}&\Bigg\{\sum_{\tilde{q}\in\{0,1\}}\int_0^\infty\frac{ds}{s^{3/2}}e^{-s(E_{\tilde{q}}+\kappa\mu)^2}\\ &+2\sum_{\tilde{q}\in\{+(1/2),-(1/2)\}}\int_0^\infty\frac{ds}{s^{3/2}}e^{-sE^{(\kappa)2}_{\tilde{q}}}\Bigg\}\\ &\times\left[1+2\sum_{\ell=1}^{\infty}(-1)^\ell e^{-(\beta^2\ell^2/4s)}\right],\end{aligned} \tag{2.20}$$

where $E_{\tilde{q}}$ are defined in (2.17). Replacing, at this stage, the discrete sum over momenta with continuous integrations over momenta by making use of

---

[4] In imaginary-time formulation, the four-dimensional space-time volume $\mathcal{V}$ is replaced by $\mathcal{V}\to V\beta$, where V is the three-dimensional space volume, and $\beta=1/T$ the compactification radius of the imaginary-time coordinate.

$$\frac{1}{V}\sum_{\mathbf{p}} f(\bar{\mathbf{p}}_{\tilde{q}=0}) \to \int \frac{d^3p}{(2\pi)^3} f(\mathbf{p}) \tag{2.21}$$

for neutral, and

$$\frac{1}{V}\sum_{\mathbf{p}} f(\bar{\mathbf{p}}_{\tilde{q}\neq 0}) \to |\tilde{q}\,\tilde{e}\,B| \sum_{n=0}^{+\infty} \alpha_n \int_{-\infty}^{+\infty} \frac{dp_3}{8\pi^2} f(n, p_3) \tag{2.22}$$

for charged particles,[5] and eventually adding the tree-level part of the effective potential to the resulting expression, the full mean-field effective potential at the one-loop level is given by[6]

$$\begin{aligned}\Omega_{\text{eff}}(\tilde{e}B, T, \mu) = {} & \frac{\sigma^2}{4G_S} + \frac{|\Delta|^2}{4G_D} + \frac{B^2}{2} \\ & + \frac{1}{2\sqrt{\pi}} \sum_{\kappa=\pm 1} \bigg\{ \int \frac{d^3p}{(2\pi)^3} \int_0^\infty \frac{ds}{s^{3/2}} e^{-s(E_0+\kappa\mu)^2} \\ & + \tilde{e}B \sum_{n=0}^{\infty} \alpha_n \int_0^\infty \frac{ds}{s^{3/2}} \int_0^\infty \frac{dp_3}{4\pi^2} \\ & \times \Big(e^{-s(E_{+1}+\kappa\mu)^2} + 2e^{-sE^{(\kappa)2}_{|\pm 1/2|}}\Big)\bigg\} \\ & \times \bigg[1 + 2\sum_{\ell=1}^{\infty} (-1)^\ell e^{-(\beta^2\ell^2/4s)}\bigg]. \end{aligned} \tag{2.23}$$

Note that, in (2.22), as well as (2.23), n denotes the discrete Landau levels, and $\alpha_n = 2 - \delta_{n0}$ is introduced to consider the fact that Landau levels with $n > 0$ are doubly degenerate [12,14]. Moreover, we have used $E_{+1/2} = E_{-1/2}$. In the next section, we will use (2.23) to determine numerically the chiral and diquark gaps and to present the complete phase structure of the magnetized two-flavor superconducting NJL model at finite T and μ.

III. NUMERICAL RESULTS

In the previous section, we have determined the effective potential (2.23) of the two-flavor NJL model, including meson and diquark condensates at finite temperature, chemical potential, and in the presence of constant magnetic fields in the mean-field approximation at one-loop level. It is the purpose of this paper to have a complete understanding of the effect of these external parameters on the quark matter in the 2SC phase. This will complete our analysis in [16], where only the effects of μ and $\tilde{e}B$ were considered at $T = 0$. We start this section with presenting the numerical results on the μ, T, and $\tilde{e}B$ dependence of the chiral and diquark condensates. We, then, continue with exploring the $T - \mu$, $T - \tilde{e}B$, and $\mu - \tilde{e}B$ phase diagrams for fixed values of $\tilde{e}B$, μ, and T, respectively. Before presenting our results, we will fix, in the subsequent paragraphs, our notations and describe our numerical method.

To determine the chiral and diquark gaps, the thermodynamic potential Ω_{eff} from (2.23) is to be minimized. To solve the corresponding gap equations

$$\frac{\partial \Omega_{\text{eff}}(\sigma, \Delta; T, \mu, \tilde{e}B)}{\partial \sigma}\bigg|_{\sigma_B, \Delta_B} = 0 \quad \text{and} \quad \frac{\partial \Omega_{\text{eff}}(\sigma, \Delta; T, \mu, \tilde{e}B)}{\partial \Delta}\bigg|_{\sigma_B, \Delta_B} = 0 \tag{3.1}$$

numerically, we have to fix the free parameters of the model. Our specific choice of the parameters is [16,33]

$$\Lambda = 0.6533\ \text{GeV}, \qquad G_S = 5.0163\ \text{GeV}^{-2}, \quad \text{and} \quad G_D = \tfrac{3}{4}G_S, \tag{3.2}$$

where Λ is the momentum cutoff, and G_S and G_D are the chiral and diquark couplings. Using this special set of parameters, we have shown in [16] that, at $T = 0$, no mixed phase, characterized with $(\sigma_B \neq 0, \Delta_B \neq 0)$, will appear. The same feature persists at finite T. Moreover, for vanishing magnetic field $\tilde{e}B = 0$ and at zero temperature, the parameters in (3.2) yield the meson mass $\sigma_0 \simeq 323.8$ MeV at $\mu = 250$ MeV and the diquark mass $\Delta_0 \simeq 126$ MeV at $\mu = 460$ MeV [16].[7] To perform the momentum integration over $\mathbf{p}$ and p_3 in (2.23) numerically, we have introduced, as in [16], smooth cutoff functions (form factors)

$$f_\Lambda = \frac{1}{1 + \exp(\frac{|\mathbf{p}|-\Lambda}{A})} \quad \text{and} \quad f^n_{\Lambda,B} = \frac{1}{1 + \exp(\frac{\sqrt{p_3^2 + 2|\tilde{q}\,\tilde{e}\,B|n} - \Lambda}{A})}, \tag{3.3}$$

which correspond to neutral and charged particles, respectively.[8] In (3.3), A is a free parameter and is chosen to be $A = 0.05\Lambda$. A similar smooth cutoff function (form factor) is also used in [13]. Here, as in [13], the free parameter A determines the sharpness of the cutoff scheme. At this stage, let us notice that the solutions of (3.1) are, in general, "local" minima of the theory. Keeping $(\sigma, \Delta) \neq (0, 0)$ and looking for "global" minima of the system described by complete $\Omega_{\text{eff}}(\sigma, \Delta; T, \mu, \tilde{e}B)$ from (2.23), it turns out that, in the regime $\mu \in [0, 800]$ MeV, $T \in [0, 250]$ MeV, and $\tilde{e}B \in [0, 0.8]$ GeV^2, the system exhibits two global

---

[5] Only charged particles interact with the external magnetic field.

[6] In [16], the same effective potential (2.23) was determined using a different method {see (3.19)–(3.22) in [16]}.

[7] Although our free parameters Λ, G_D, and G_S coincide with the parameters used in [33], the numerical value of σ_0 is different from what is reported in [33]. The reason for this difference is apparent in the choice of the cutoff function. Whereas, in [33], a sharp momentum cutoff is used, we have used a smooth cutoff function (3.3) to perform the momentum integrations numerically.

[8] In (2.23), the integrals proportional to $\tilde{e}B$ and including a summation over Landau levels n arise from charged quarks with charges $\tilde{q} = \pm\frac{1}{2}, +1$.

minima. They are given by $(\sigma_B \neq 0, \Delta_B = 0)$ and $(\sigma_B \neq 0, \Delta_B = 0)$. We will denote the regime characterized by these two global minima by the χSB and the CSC phases, respectively. According to the above descriptions, in order to determine the chiral and diquark condensates, we will use, instead of the gap equations (3.1),

$$\frac{\partial\Omega_{\text{eff}}(\sigma, \Delta_B = 0; T, \mu, \tilde{e}B)}{\partial\sigma}\bigg|_{\sigma_B} = 0 \qquad (3.4)$$

in the χSB phase and

$$\frac{\partial\Omega_{\text{eff}}(\sigma_B = 0, \Delta; T, \mu, \tilde{e}B)}{\partial\Delta}\bigg|_{\Delta_B} = 0 \qquad (3.5)$$

in the CSC phase to simplify our computations. As it turns out, apart from the χSB and the CSC phases, there is also a normal phase characterized by $(\sigma_B = 0, \Delta_B = 0)$. Following the method presented in [20], we will determine the critical lines of first-order transition between the χSB phase and the normal phase using

$$\frac{\partial\Omega_{\text{eff}}(\sigma, \Delta_B = 0)}{\partial\sigma}\bigg|_{\sigma_B} = 0 \quad \text{and}$$
$$\Omega_{\text{eff}}(\sigma_B, \Delta_B = 0) = \Omega_{\text{eff}}(\sigma_B = 0, \Delta_B = 0). \qquad (3.6)$$

Similarly, the first-order phase transition between the χSB and the CSC phases is determined by solving

$$\begin{aligned} \frac{\partial\Omega_{\text{eff}}(\sigma, \Delta_B = 0)}{\partial\sigma}\bigg|_{\sigma_B} &= 0, \\ \frac{\partial\Omega_{\text{eff}}(\sigma_B = 0, \Delta)}{\partial\Delta}\bigg|_{\Delta_B} &= 0, \end{aligned} \qquad (3.7)$$

and

$$\Omega_{\text{eff}}(\sigma_B = 0, \Delta_B) = \Omega_{\text{eff}}(\sigma_B, \Delta_B = 0), \qquad (3.8)$$

simultaneously [20]. The second-order critical lines between the χSB and CSC phases and the normal phase will be also determined by the method described in [20] (see Eq. (2.35) in [20]): To determine the second-order critical line between the χSB and the normal phase, we solve

$$\lim_{\sigma^2 \to 0} \frac{\partial\Omega_{\text{eff}}(\sigma, \Delta = 0)}{\partial\sigma^2} = 0. \qquad (3.9)$$

The second-order critical line between the CSC and the normal phase is, then, determined by solving

$$\lim_{\Delta^2 \to 0} \frac{\partial\Omega_{\text{eff}}(\sigma = 0, \Delta)}{\partial\Delta^2} = 0. \qquad (3.10)$$

The same method is also used in [21] to find the second-order phase transition between the χSB and the normal phase (see page 9 in [21]). To make sure that, after the second-order phase transition, the global minima of the effective potential are shifted to $\sigma = 0$ in (3.9) and to $\Delta = 0$ in (3.10), and in order to avoid instabilities, an analysis similar to [9] is also performed. The same method is also used in [16] to determine the second-order critical line between the CSC and the normal phase.

A. The $(\mu, T, \tilde{e}B)$ dependence of chiral and diquark condensates

1. *The μ dependence of σ_B and Δ_B*

The μ dependence of both gaps at different temperatures, $T = 0, 20, 70, 150$ MeV, and magnetic fields, $\tilde{e}B = 0, 0.3, 0.5$ GeV^2, is demonstrated in Figs. 1–4, panels (a)–(c), respectively. The green dashed and solid lines denote the σ_B mass gaps. The red solid lines determine the normal phase with $\sigma_B = \Delta_B = 0$. The diquark gaps Δ_B are demonstrated with blue solid lines. Dashed (solid) lines denote the first- (second-) order phase transitions.

The plots in Figs. 1(a)–1(c) show that, at $T = 0$ MeV, the magnetic field enhances the formation of the chiral condensate σ_B. The value of σ_B is constant in μ, with $\mu < \mu_c$ and $\mu_c \simeq 320$–350 MeV, and increases with $\tilde{e}B$. On the other hand, for small values of $\tilde{e}B < 0.5$ GeV^2, Δ_B increases with μ in the regime $\mu_c < \mu < 600$ MeV [Figs. 1(a) and 1(b)]. A similar observation is also made in [16], where the same model as in the present paper is studied, and, additionally, the color-chemical potential μ_8 is assumed to be nonzero. Comparing the diagrams in Fig. 1 with the corresponding diagrams in Fig. 7 of [16], it turns out that μ_8 has no significant effect on the μ dependence of σ_B and Δ_B at $T = 0$ MeV.[9] For $\tilde{e}B = 0$ GeV^2, the μ dependence of the diquark mass gap in Fig. 1(a) can be compared with the analytical result

$$\Delta_0^2 = \mathcal{C}_2(\Lambda^2 - \mu^2)\exp\left[-\frac{\Lambda^2}{\mu^2}\left(\frac{1}{\hat{g}_d} - 1\right)\right] \qquad (3.11)$$

from [16]. In (3.11), $\mathcal{C}_2 = 4e^{-3} \simeq 0.2$, and $\hat{g}_d \equiv \frac{4G_D\Lambda^2}{\pi^2}$. Plugging the numerical values of Λ and G_D from (3.2) into (3.11) and plotting the resulting expression in a Δ_0 vs μ diagram, the result is in close agreement with the μ dependence of the diquark mass gap in Fig. 1(a) in the regime $320 < \mu < 600$ MeV. In the same regime of μ, the μ dependence of Δ_0 from (3.11) agrees also with the well-known result from [36]. In contrast, as it can be seen in Fig. 1(c), for $\tilde{e}B = 0.5$ GeV^2, Δ_B decreases with $\mu \in [350, 600]$ GeV. This behavior is expected from the analytical expression

$$\Delta_B^2 = 4(\Lambda_B^2 - \mu^2)\exp\left(-\frac{\Lambda^2}{\Lambda_B^2}\frac{1}{g_d}\right), \qquad (3.12)$$

which is also computed in [16] using an appropriate LLL approximation.[10] In (3.12), $\Lambda_B \equiv \sqrt{\tilde{e}B}$ and $g_d \equiv \frac{G_D\Lambda^2}{\pi^2}$. Plugging the numerical values of Λ and G_D from (3.2) into

---

[9] In [34], in the $\tilde{e}B = 0$ case, the color-chemical potential μ_8 is shown to be small, and its effect is, therefore, neglected. See also [35], where two-flavor magnetized color-superconducting quark matter with $\mu_8 = 0$ is studied.

[10] Later, we will see that $\tilde{e}B \simeq 0.5$ GeV^2 is strong enough to justify a LLL approximation.

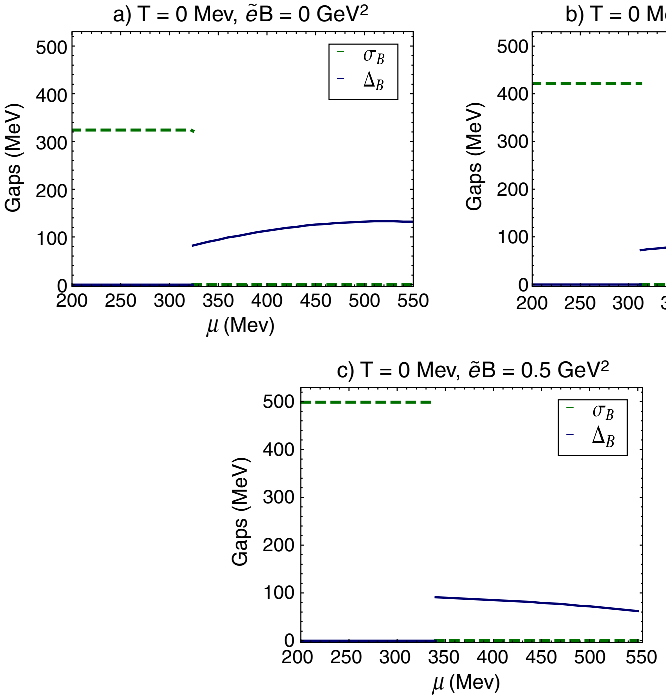

FIG. 1 (color online). The μ dependence of σ_B (dashed green lines) and Δ_B (solid blue lines) is demonstrated for $T = 0$ MeV and $\tilde{e}B = 0, 0.3, 0.5\ \mathrm{GeV}^2$ in (a), (b), and (c), respectively. The transitions from the χSB, characterized by ($\sigma_B \neq 0$, $\Delta_B = 0$), to the CSC phase, characterized by ($\sigma_B = 0$, $\Delta_B \neq 0$), are of first order.

(3.12) and plotting the resulting expression in a Δ_B vs μ diagram for $\tilde{e}B = 0.5\ \mathrm{GeV}^2$, it turns out that Δ_B decreases with μ in the regime $350 < \mu < 600$ MeV, as it is shown in Fig. 1(c). A similar expression to (3.12) is also derived in [11] for the diquark mass gap in a three-flavor CFL model in the presence of a strong magnetic field, using the LLL approximation.

In Figs. 2(a)–2(c), the μ dependence of σ_B and Δ_B is plotted at $T = 20$ MeV and for $\tilde{e}B = 0, 0.3, 0.5\ \mathrm{GeV}^2$. Comparing with the results from Figs. 1(a)–1(c), it turns out that increasing temperature up to $T = 20$ MeV has no significant effects on the results of $T = 0$ MeV. This is in contrast with the situation at $T = 70$ MeV. In Figs. 3(a)–3(c), the μ dependence of σ_B and Δ_B is plotted at $T = 70$ MeV and for $\tilde{e}B = 0, 0.3, 0.5\ \mathrm{GeV}^2$. As it turns out, in the regime $\mu < \mu_c$, the chiral condensate σ_B increases with the magnetic field. The diquark condensate appears in the regime $\mu \in [480, 600]$ MeV for $\tilde{e}B = 0, 0.3\ \mathrm{GeV}^2$ [Figs. 3(a) and 3(b)]. For $\tilde{e}B = 0.5\ \mathrm{GeV}^2$, in Fig. 3(c), however, no diquark condensate appears in the relevant regime $\mu < 600$ MeV. Moreover, comparing Figs. 2 and 3, we notice that at $T = 70$ MeV, in Fig. 3, in contrast to the situation at $T = 20$ MeV, in Fig. 2, the first-order transition from the χSB to the normal phase does not occur over the CSC phase. In Fig. 3, for $\tilde{e}B < 0.5\ \mathrm{GeV}^2$, there is a first-order phase transition from the χSB to the normal phase; then, a second-order phase transition occurs from the normal to the CSC phase. For $\tilde{e}B = 0.5\ \mathrm{GeV}^2$, the phase transition from the χSB to the normal phase is of first order, but no CSC phase appears in the regime $\mu < 600$ MeV.

At higher temperature, as it is demonstrated for $T = 150$ MeV in Fig. 4, no diquark condensate appears at all in the relevant regime $\mu < 600$ MeV [Figs. 4(a)–4(c)]. Moreover, whereas for $\tilde{e}B = 0, 0.3\ \mathrm{GeV}^2$, the transitions from the χSB to the normal phase are of second order, for $\tilde{e}B = 0.5\ \mathrm{GeV}^2$, the χSB-normal phase transition turns out to be of first order. The above observations suggest that, while the magnetic field catalyzes the formation of the chiral condensate σ_B, the diquark condensate Δ_B is suppressed in the presence of a constant magnetic field. However, as it turns out, the latter feature depends on the strength of the magnetic field. This will be shown explicitly in the next section, where the effect of arbitrary magnetic fields on the formation of σ_B and Δ_B for a wide range of $\tilde{e}B \in [0, 0.8]\,\mathrm{GeV}^2$ will be explored.

2. The $\tilde{e}B$ dependence of σ_B and Δ_B

The effect of external magnetic fields on the formation of chiral condensates is studied intensively in the literature (see, e.g., [1,17–19]). As it is shown in [1], in the presence of strong magnetic fields, the dynamics of the system are fully described by its dynamics in the LLL. However, there is, to the best of our knowledge, no evidence in the literature that fixes quantitatively the strength of a magnetic field that is enough to justify a LLL approximation. In [16], we have answered this question numerically. First,

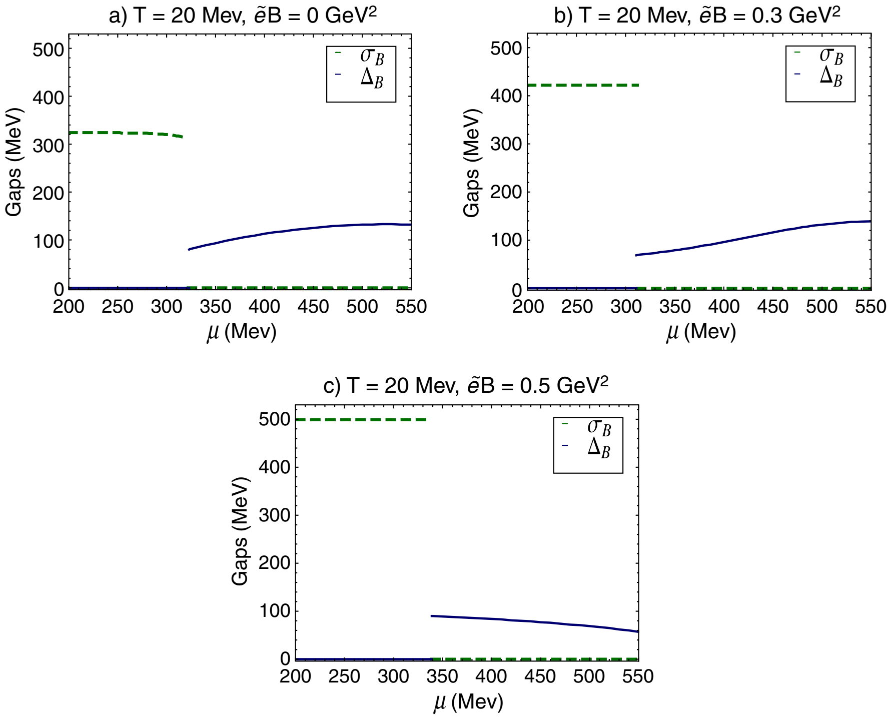

FIG. 2 (color online). The μ dependence of σ_B (dashed green lines) and Δ_B (solid blue lines) is demonstrated for $T = 20$ MeV and $\tilde{e}B = 0, 0.3, 0.5$ GeV^2 in (a), (b), and (c), respectively. The transitions from the χSB phase, characterized by ($\sigma_B \neq 0$, $\Delta_B = 0$), to the CSC phase, characterized by ($\sigma_B = 0$, $\Delta_B \neq 0$), are of first order.

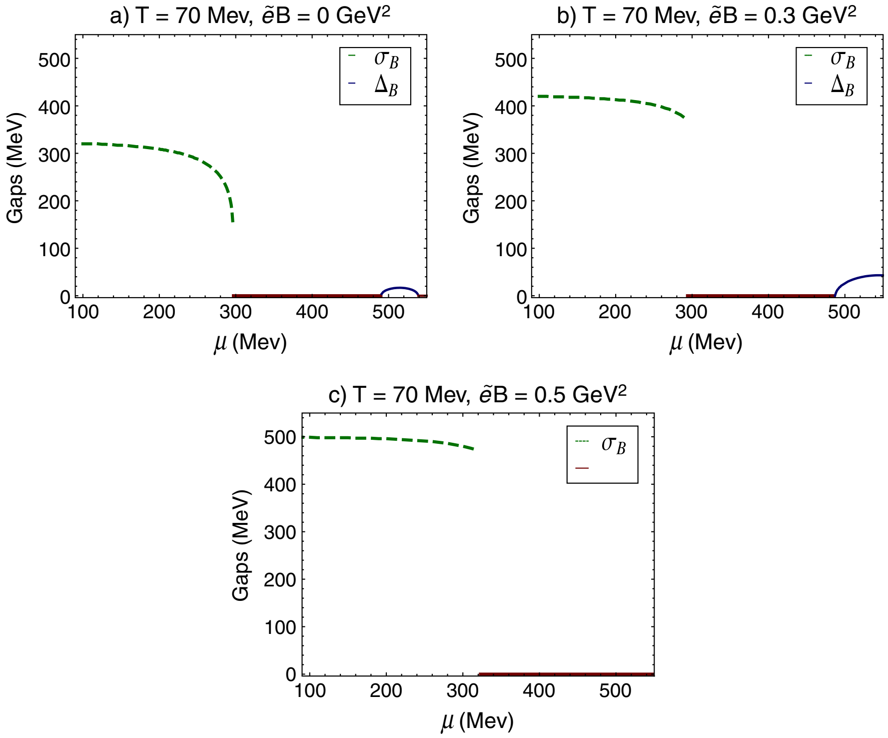

FIG. 3 (color online). The μ dependence of σ_B (dashed green curved lines) and Δ_B (solid blue curved lines) is demonstrated for $T = 70$ MeV and $\tilde{e}B = 0, 0.3$ GeV^2 in (a) and (b), respectively. While the transitions from the χSB to the normal phase (solid straight red line) are of first order, the transitions from the normal to the CSC phase are of second order. Note that the χSB, CSC, and normal phases are characterized by ($\sigma_B \neq 0$, $\Delta_B = 0$), ($\sigma_B = 0$, $\Delta_B \neq 0$), and ($\sigma_B = 0$, $\Delta_B = 0$), respectively. (c) The μ dependence of σ_B is demonstrated for $T = 70$ MeV and $\tilde{e}B = 0.5$ GeV^2. The transition from the χSB to the normal phase is of first order. No CSC phase appears at $\mu > 330$ MeV.

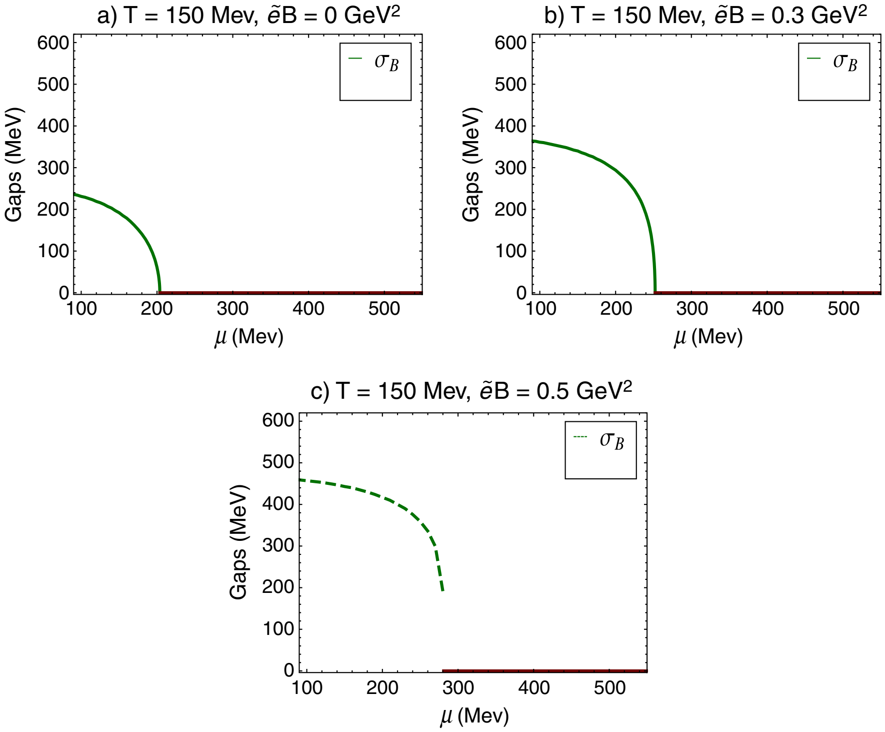

FIG. 4 (color online). The μ dependence of σ_B (dashed and solid green curved lines) is demonstrated for $T = 150$ MeV and $\tilde{e}B = 0, 0.3, 0.5$ GeV^2 in (a)–(c). While, for $\tilde{e}B = 0, 0.3$ GeV^2, the transition from χSB to the normal phase (solid straight red line) is of second order (solid green curved line), for $\tilde{e}B = 0.5$ GeV^2, this transition is of first order (dashed green curved line). No CSC phase appears at $T = 150$ MeV. Note that the χSB, CSC, and normal phases are characterized by ($\sigma_B \neq 0$, $\Delta_B = 0$), ($\sigma_B = 0$, $\Delta_B \neq 0$), and ($\sigma_B = 0$, $\Delta_B = 0$), respectively.

we have determined the $\tilde{e}B$ dependence of the gaps in a LLL approximation and, then, compared the analytical results with the numerical ones, including the effect of all Landau levels. It turned out that, by increasing the magnetic field from $\tilde{e}B = 0$ GeV^2 to $\tilde{e}B = 0.8$ GeV^2, first in the regime $\tilde{e}B < 0.45$ GeV^2, the mass gaps underlie small van Alphen-de Haas oscillations. Above a certain threshold magnetic field $\tilde{e}B_t \simeq 0.45$–0.50 GeV^2, the dependence of the condensates of $\tilde{e}B$ was linear. In this linear regime, our numerical results were comparable with the analytical results arising from the solution of the corresponding gap equations in the LLL approximation.

In Fig. 5, the $\tilde{e}B$ dependence of meson and diquark mass gaps, σ_B and Δ_B, is plotted at $T = 0$ and $\mu = 250$ MeV [Fig. 5(a)] and $\mu = 460$ MeV [Fig. 5(b)]. A comparison with similar plots from Fig. 2 of [16] shows that a color-neutrality condition has no significant effect on the above-mentioned threshold magnetic field $\tilde{e}B_t \simeq 0.5$ GeV^{2}or on the behavior of the σ_B and Δ_B below and above $\tilde{e}B_t$, consisting of van Alphen-de Haas oscillations in $\tilde{e}B < \tilde{e}B_t$ and the linear rise in $\tilde{e}B > \tilde{e}B_t$ regimes.[11] A similar strong van Alphen-de Haas oscillation of the 2SC mass gap Δ_B in the regime $\tilde{e}B \in [0.4, 0.6]$ GeV^2 in Fig. 5(b) is also observed in [13,14] in the three-flavor CFL phase in the presence of magnetic fields, albeit in another regime of $\tilde{e}B/\mu^2$.

In Fig. 6(a), the $\tilde{e}B$ dependence of σ_B is demonstrated for fixed $\mu = 250$ MeV and at various fixed temperatures $T = 20, 60, 70$ MeV; after small oscillations in the regime below the threshold magnetic field $\tilde{e}B_t$, the system enters the linear regime, where only the contribution of the LLL affects the dynamics of the system. For $\tilde{e}B < \tilde{e}B_t$, σ_B decreases by increasing the temperature. In the linear regime $\tilde{e}B > \tilde{e}B_t$, however, the effect of temperature is minimized. In Fig. 6(b), the dependence of the diquark gap Δ_B is demonstrated for fixed $\mu = 460$ MeV and at various temperatures $T = 20, 60, 70$ MeV. At $T = 20$ MeV, small oscillations occur in $\tilde{e}B < \tilde{e}B_t$. In contrast, Δ_B monotonically increases with $\tilde{e}B$ in the linear regime $\tilde{e}B > \tilde{e}B_t$. The behavior of Δ_B at $T = 20$ MeV is not too much different than its behavior at $T = 0$ MeV [see Fig. 5(b)]. This confirms our previous observation from the comparison of Figs. 1 and 2. By increasing the temperature to $T = 60$ MeV, Δ_B decreases. It vanishes in the range $\tilde{e}B \in [0.4, 0.6]$ GeV^2. Comparing to the $T = 0$ MeV plot from Fig. 5(b), it turns out that the value of Δ_B at $T = 0$ MeV in this regime of $\tilde{e}B \in [0.4, 0.6]$ GeV^2 is in the same order of magnitude as 60 MeV. This is related with the well-known BCS ratio of the critical-temperature to zero-temperature gap in the zero magnetic field case

---

[11] See footnote 9.

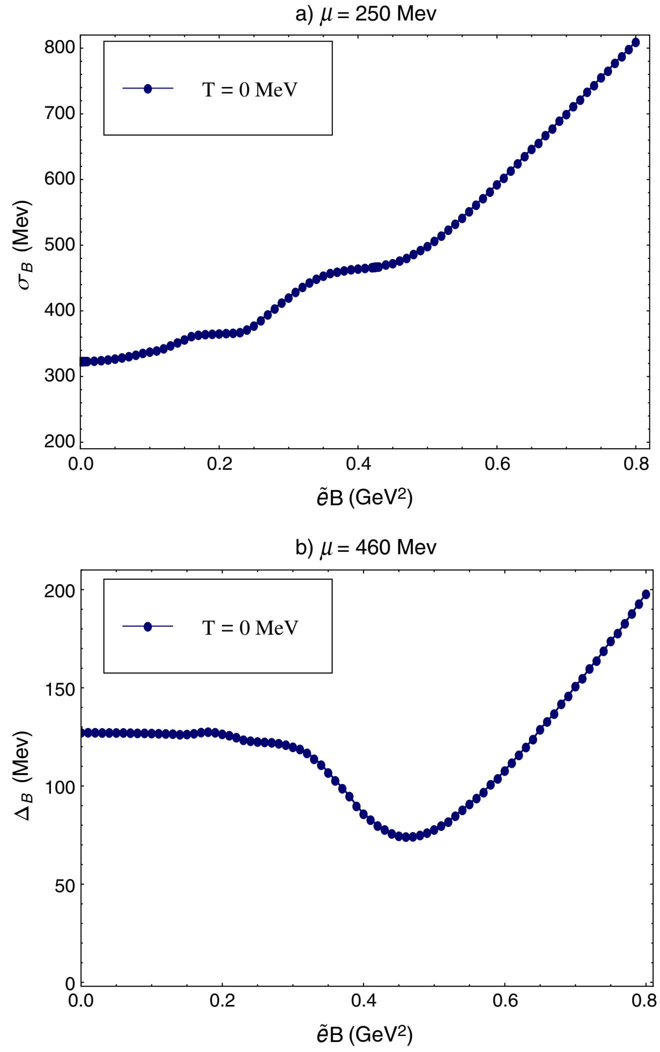

FIG. 5 (color online). (a) The dependence of the chiral gap σ_B on $\tilde{e}B$ for fixed $\mu = 250$ MeV, at $T = 0$ MeV. (b) The dependence of the diquark gap Δ_B on $\tilde{e}B$ for fixed $\mu = 460$ MeV, at $T = 0$ MeV.

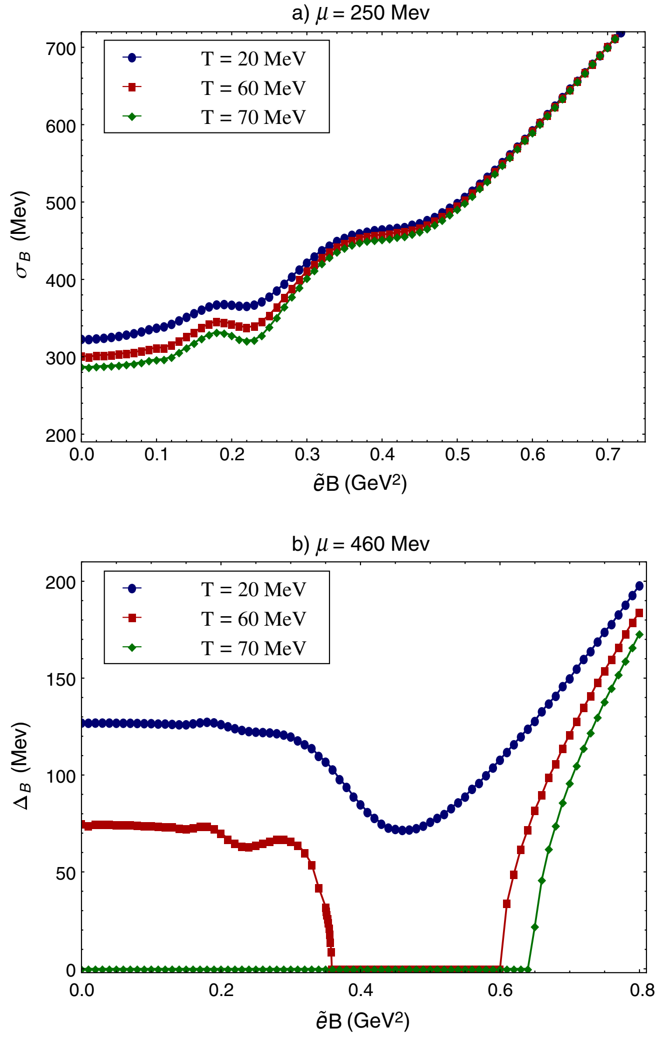

FIG. 6 (color online). (a) The dependence of the chiral gap σ_B on $\tilde{e}B$ for fixed $\mu = 250$ MeV, at various temperatures. (b) The dependence of the diquark gap Δ_B on $\tilde{e}B$ for fixed $\mu = 460$ MeV, at various temperatures.

[37] (see the discussion below). For $\tilde{e}B > 0.6$ GeV^2, Δ_B increases again with $\tilde{e}B$. The situation demonstrated in Fig. 6(b) at $T = 60$ MeV can be interpreted as a second-order phase transition from the CSC to the normal phase at $T = 60$ MeV, $\mu = 460$ MeV, and $\tilde{e}B \simeq 0.4$ GeV^2, followed up with a second-order phase transition from the normal to the CSC phase at $T = 60$ MeV, $\mu = 460$ MeV, and $\tilde{e}B \simeq 0.6$ GeV^2. We believe that this CSC-Normal-CSC phase transition is caused by strong van Alphen-de Haas oscillations in the regime $\tilde{e}B \in [0.4, 0.6]$ GeV^2. A comparison between the $T = 60$ MeV plot of Fig. 6(b) and the $\mu = 460$ MeV plot of Fig. 14(i) confirms these statements.[12] Let us notice that van Alphen-de Haas oscillations, which are also observed in metals [29], are the consequence of oscillatory structure in the density of states of quarks and occur whenever the Landau level passes the quark Fermi surface [14,21].

In Fig. 6(b), at $T = 70$ MeV and in the regime for $\tilde{e}B \lesssim \tilde{e}B_t$, the diquark condensate is not built at all, i.e., $\Delta_B = 0$. This result indicates that a normal phase exists at $T \geq 70$ MeV, $\mu = 460$ MeV, and in the regime $\tilde{e}B \lesssim 0.65$ GeV^2, and that a second-order phase transition from the normal to the CSC phase occurs at $(T, \mu) \sim (70, 460)$ MeV and the critical magnetic field $\tilde{e}B \simeq 0.65$ GeV^2. These results coincide with the observations in the complete $T - \tilde{e}B$ phase diagram from Fig. 14(i) for $\mu = 460$ MeV. Indeed, our numerical computations show that, for $\mu = 460$ MeV, the critical temperatures in the whole range of $\tilde{e}B \in [0, 0.6]$ GeV^2 are smaller than 70 MeV. In $\tilde{e}B = 0$ GeV^2 and $\mu = 460$ MeV, it is $T_c \simeq 68.5$ MeV and decreases with $\tilde{e}B \lesssim 0.5$ GeV^2 [see also

---

[12] See also the explanations in Sec. III B 2, where a more detailed comparison will be presented between the results of Fig. 14 and Fig. 6.

Fig. 14(i)]. Using this value of T_c in the zero magnetic field and the numerical value of the diquark gap at zero temperature and zero magnetic field from Fig. 5(b), i.e., $\Delta_B(T=0) \simeq 127.5$ MeV, the above-mentioned BCS ratio can be computed. It is given by

$$\frac{T_c}{\Delta_B(T=0)} \simeq \frac{68.5}{127.5} \simeq 0.54,$$

which is in good agreement with the BCS ratio $\frac{T_c}{\Delta_B(T=0)} = e^{\gamma}\pi^{-1} + \mathcal{O}(g) \simeq 0.567 + \mathcal{O}(g)$ of critical temperature to the zero-temperature 2SC mass gap of QCD in the zero magnetic field [37]. Here, $\gamma \simeq 0.577$ is the Euler-Mascheroni constant. As for the regime of strong magnetic fields, for $\tilde{e}B > 0.6$ GeV^2 and fixed $T = 70$ MeV, Δ_B increases monotonically with $\tilde{e}B$, as expected from (3.12) for $\mu = 460$ MeV, and for Λ and G_D from (3.2).

In Fig. 7, the dependence of chiral and diquark gaps on the external magnetic field for constant T is demonstrated for various μ. As it is shown in Fig. 7(a), the chiral mass gap σ_B decreases by increasing μ. Small van Alphen-de Haas oscillations occur in the regime below the threshold magnetic field $\tilde{e}B_t \simeq 0.5$ GeV^2 and die out in the linear regime above $\tilde{e}B_t$. In this regime, σ_B monotonically rises with $\tilde{e}B$, and the effect of μ is minimized. In the regime below $\tilde{e}B_t$, for $\mu = 300$ MeV, the chiral mass gap σ_B vanishes. This indicates a first-order phase transition from the normal into the χSB phase at fixed $T = 100$ MeV, $\mu = 300$ MeV, and for $\tilde{e}B \simeq 0.5$ GeV^2. This result agrees with our findings from the complete $T - \tilde{e}B$ phase diagram plotted in Fig. 14(c) for fixed $\mu = 300$ MeV. As it can be checked in Fig. 14(c), at fixed $T = 100$ MeV, the χSB phase appears first for $\tilde{e}B > 0.5$ GeV^2. As concerns the $\tilde{e}B$ dependence of the diquark mass gap in Fig. 7(b), it increases with μ in the regime below the threshold magnetic field $\tilde{e}B_t$. In the regime above $\tilde{e}B_t$, however, Δ_B decreases by increasing μ. The same phenomenon was also demonstrated in Fig. 2(c) at the low temperature $T = 20$ MeV and for $\tilde{e}B = 0.5$ near $\tilde{e}B_t$, and was shown to be in full agreement with the analytical result (3.12) [16]. Note that strong van Alphen-de Haas oscillations are responsible for vanishing Δ_B in the regime $\tilde{e}B \in [0.4, 0.6]$ GeV^2. They induce CSC-Normal-CSC second-order phase transitions, as it can be seen in the same regime of $\tilde{e}B$ in Fig. 14(i). The plots in Fig. 7(b) show also that the critical magnetic fields for the transition from the normal into the CSC phase increase by increasing the chemical potential [see Fig. 7(b)].[13]

3. The T dependence of σ_B and Δ_B

In Fig. 8, the temperature dependence of the chiral condensate is presented for fixed $\mu = 250$ MeV [panel (a)], $\mu = 300$ MeV [panel (b)], and various

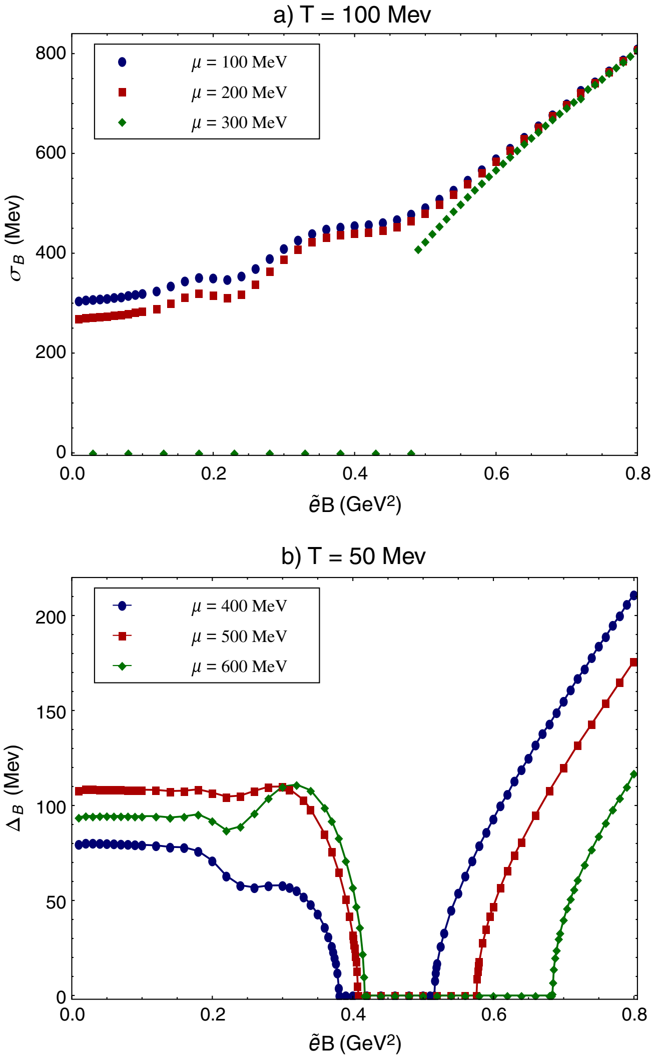

FIG. 7 (color online). (a) The dependence of the chiral gap σ_B on $\tilde{e}B$ for fixed $T = 100$ MeV, at various chemical potentials μ. (b) The dependence of the diquark gap Δ_B on $\tilde{e}B$ for fixed $T = 50$ MeV, at various chemical potentials.

magnetic fields $\tilde{e}B = 0, 0.3, 0.5$ GeV^2. Whereas the transition from the χSB into the normal phase for $\mu = 250$ MeV is of second order [continuous decreasing of σ_B to $\sigma_B = 0$ in Fig. 8(a)], it is of first order for $\mu = 300$ MeV [discontinuous transition from $\sigma_B \neq 0$ to $\sigma_B = 0$ in Fig. 8(b)]. As it is also expected from our previous results, the magnetic field enhances the production of σ_B, so that it increases by increasing the value of the magnetic field.

The temperature dependence of Δ_B is presented in Fig. 9 for fixed $\mu = 480$ MeV and $\tilde{e}B = 0, 0.4, 0.5$ GeV^2 [panel (a)] below the threshold magnetic field $\tilde{e}B_t \simeq 0.45$–0.50 GeV^2, as well as for fixed $\mu = 480$ MeV and $\tilde{e}B = 0.6, 0.7, 0.8$ GeV^2 above the threshold magnetic field. As it turns out, magnetic fields below the threshold magnetic field suppress the production of Δ_B, whereas magnetic fields stronger than the threshold magnetic field

---

[13] Detailed analysis on the dependence of critical $\tilde{e}B$ on μ and vice versa will be performed in Sec. III B.

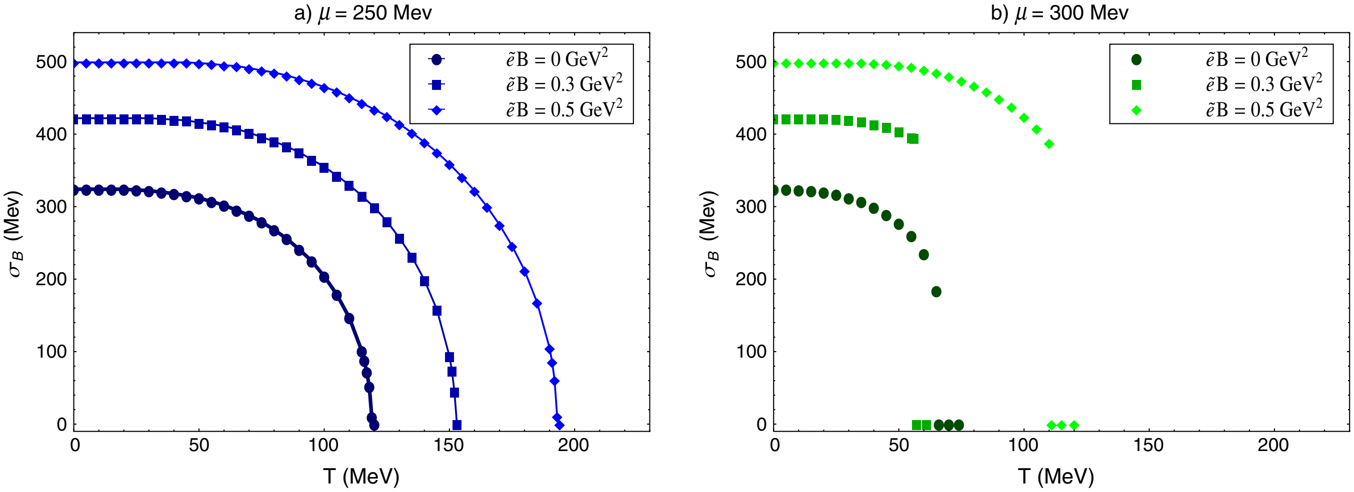

FIG. 8 (color online). The T dependence of σ_B for fixed $\mu = 250$ MeV [panel (a)] and $\mu = 300$ MeV [panel (b)] for various $\tilde{e}B = 0, 0.3, 0.5$ GeV^2. Whereas for $\mu = 250$ MeV, the transition from the chiral to the normal phase is of second order [continuous decreasing of σ_B to $\sigma_B = 0$ in panel (a)], for $\mu = 300$ MeV, this transition is of first order [discontinuous transition from $\sigma_B \neq 0$ to $\sigma_B = 0$ in panel (b)].

enhance its production [see also Fig. 6(b)]. Similarly, for $\tilde{e}B < \tilde{e}B_t$, the value of critical temperature decreases by increasing the magnetic field, whereas for $\tilde{e}B > \tilde{e}B_t$, the critical temperatures increase by increasing the magnetic field.[14]

The same effect is also observed in Fig. 10. In Fig. 10(a), the T dependence of σ_B is plotted for constant $\tilde{e}B = 0.3$ GeV^3 and various $\mu = 100, 200, 300$ MeV. At the low temperature $T < 50$ MeV, σ_B remains constant and decreases by increasing the temperature. Increasing the chemical potential only accelerates this decrease, i.e., the critical temperature decreases by increasing μ. Whereas the transition at $\mu = 100, 200$ MeV is of second order (blue bullets/rectangles), a first-order phase transition occurs at $\mu = 300$ MeV (red diamonds). The T dependence of the diquark condensate Δ_B is demonstrated for $\tilde{e}B = 0.3$ GeV^2 below the threshold magnetic field [Fig. 10(b)] and for $\tilde{e}B = 0.7$ GeV^2 above the threshold magnetic field [Fig. 10(c)]. As it turns out, whereas the diquark condensate increases by increasing μ for fixed T, and $\tilde{e}B < \tilde{e}B_t$ [Fig. 10(b)], it decreases by increasing μ for $\tilde{e}B > \tilde{e}B_t$ [Fig. 10(c)]. This result coincides with our results from Fig. 7(b). Moreover, as we can see in Figs. 10(b) and 10(c), the diquark condensates decrease by increasing the temperature. Similar to what is observed in Fig. 9, for $\tilde{e}B = 0.3$ GeV^2, below $\tilde{e}B_t$, the critical temperature increases by increasing μ [Fig. 10(b)], while for $\tilde{e}B = 0.7$ GeV^2 above $\tilde{e}B_t$, the critical temperature decreases by increasing μ. Later, we will see that this result is also in full agreement to our result from Fig. 14(i).

B. Phase diagrams of hot magnetized 2SC quark matter

To complete our study on the effect of $(T, \mu, \tilde{e}B)$ on the quark matter, including mesons and diquarks in the presence of a constant magnetic field, we will present, in this section, the phase structure of the model in a $T - \mu$ plane for various fixed $\tilde{e}B$ in Fig. 11. The $T - \tilde{e}B$ phase diagram of the model for various fixed μ will be presented in Fig. 14, and, finally, in Figs. 16 and 17, the $\mu - \tilde{e}B$ phase diagram will be explored for various fixed T. As in the previous section, green dashed lines denote the first-order phase transitions, and the blue solid lines the second-order transitions.

1. $T - \mu$ phase diagram for various fixed $\tilde{e}B$

In Fig. 11, the $T - \mu$ phase diagram of the model is demonstrated for various fixed $\tilde{e}B$. As we have argued at the beginning of this section, three different phases appear in this system: the χSB phase, the CSC phase, and the normal phase. To study the effects of constant magnetic fields on the phase transition in the $T - \mu$ plane, let us compare the plots from Fig. 11 with the plots from Figs. 2–4. As we have observed in Figs. 2(a)–2(c), at a fixed and low temperature $T < T_1$, first-order transitions occur between the χSB and the CSC phase. By increasing the temperature to $T_1 < T < T_2$, after a first-order phase transition between the χSB to the normal phase, the normal phase goes over into the CSC phase in a second-order phase transition [see 2(a) and 2(b)]. At higher temperatures $T > T_2$, no CSC phase exists. Here, depending on the strength of the external magnetic fields, only second- or first-order transitions occur between the χSB and the normal phase [Figs. 4(a)–4(c)]. As it turns out, the values of T_1 and T_2 depend on the external magnetic field, as it can be seen also in the plots from Fig. 11.

---

[14] The $\tilde{e}B$ dependence of critical temperatures will be discussed in detail in III B.

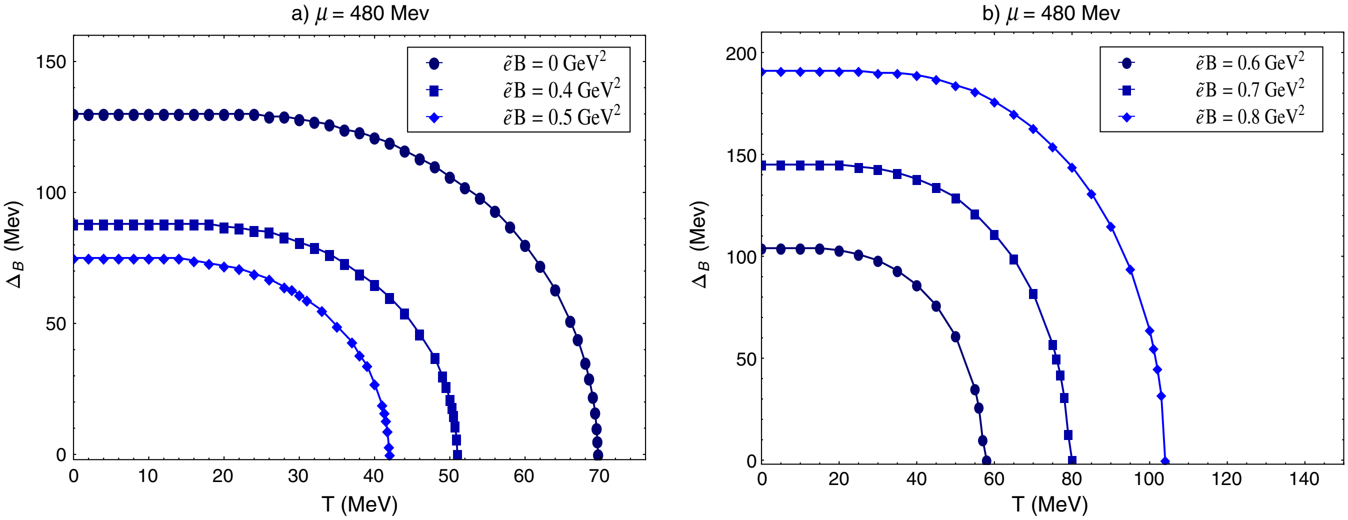

FIG. 9 (color online). The T dependence of Δ_B for fixed $\mu = 480$ MeV for various $\tilde{e}B = 0, 0.3, 0.5$ GeV^2 below the threshold magnetic field [panel (a)] and for $\tilde{e}B = 0.6, 0.7, 0.8$ GeV^2 above the threshold magnetic field [panel (b)]. Below (above) the threshold magnetic field, the production of diquarks is suppressed (enhanced).

The phase transition from the χSB to the CSC phase and from the CSC to the normal phase are always of first and second order, respectively. The order of phase transition between the χSB and the normal phase depends, however, on the value of the external magnetic field $\tilde{e}B$. To describe this effect, let us consider the blue solid lines in Fig. 11 that demonstrate the second-order phase transitions between the χSB and the normal phases. Starting from a high temperature and zero chemical potential, they all end at the critical points denoted by C (black bullets). They are, then, followed by first-order critical lines (green dashed lines) between the χSB and the normal phase. The latter start at the critical points C and end up at the tricritical points T (red bullets), where three phases coexist. In Table I, the values of the temperature and chemical potentials corresponding to the critical points ($T_{\rm cr}$, $\mu_{\rm cr}$) and the tricritical points ($T_{\rm tr}$, $\mu_{\rm tr}$) are presented.

As we can see in Fig. 11, by increasing the external magnetic field, the black bullets are shifted more and more to higher values of temperature and chemical potential (see

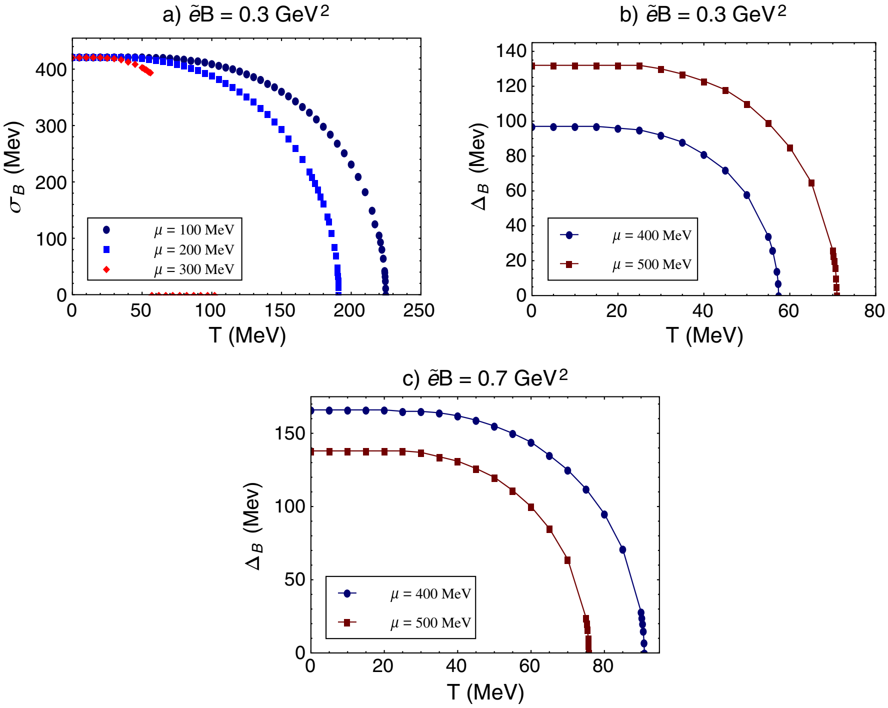

FIG. 10 (color online). T dependence of σ_B and Δ_B for different μ for fixed $\tilde{e}B$.

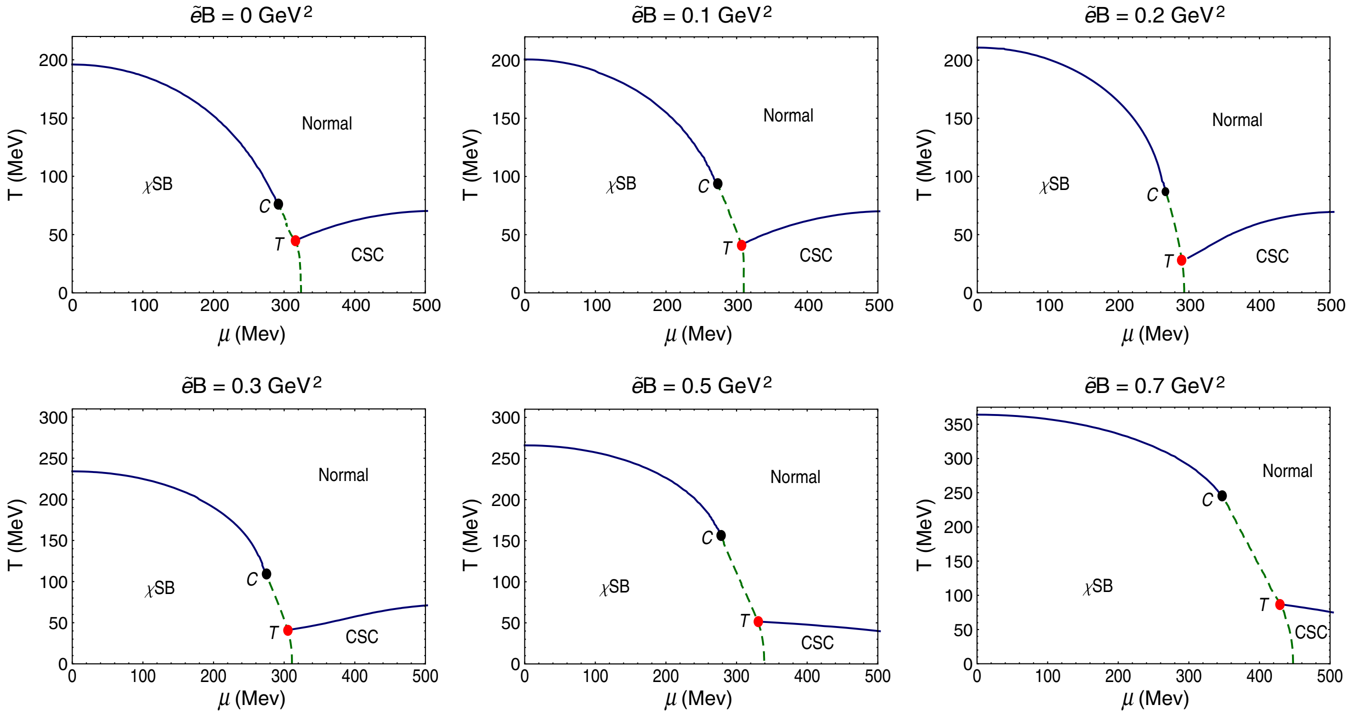

FIG. 11 (color online). The $T - \mu$ phase diagram of hot magnetized 2SC quark matter is presented for various $\tilde{e}B$. Blue solid lines denote the second-order phase transitions, and the green dashed lines the first-order transitions. The critical and tricritical points are denoted by C and T, respectively.

also the second column in Table I), so that the distance between the black and red bullets increases by increasing the strength of the external magnetic field. This is another effect of the external magnetic field; increasing the magnetic-field strength changes the type of the χSB-to-normal phase transition from second to first order. This can also be observed in Figs. 4(a)–4(c), where at high enough temperature, the χSB phase transition to the normal phase is initially of second order and, then, for larger magnetic fields, changes to a first-order phase transition.

TABLE I. Critical and tricritical points in the $T - \mu$ phase diagrams of Fig. 11, denoted by $(\mu_{\rm cr}, T_{\rm cr})$ and $(\mu_{\rm tr}, T_{\rm tr})$, respectively. Here, $\tilde{e}B$ is in GeV^2; T and μ are in MeV.

	$T - \mu$ phase diagram (Fig. 11)	
$\tilde{e}B$	$(\mu_{\rm cr}, T_{\rm cr})$	$(\mu_{\rm tr}, T_{\rm tr})$
0	(292, 76)	(316, 45)
0.01	(280, 84)	(309, 43)
0.05	(281, 87)	(315, 44)
0.10	(273, 94)	(307, 41)
0.20	(267, 87)	(290, 28)
0.30	(275, 109)	(305, 41)
0.40	(274, 141)	(320, 46)
0.50	(278, 156)	(331, 52)
0.60	(314, 189)	(377, 68)
0.70	(347, 245)	(429, 87)
0.80	(398, 271)	(479, 104)
0.90	(444, 304)	(566, 111)
1.00	(485, 345)	(581, 132)

Increasing the magnetic-field strength leads also to an increase in the values of $(\mu_{\rm tr}, T_{\rm tr})$ corresponding to the tricritical point (see the third column of Table I). This confirms the conclusion at the end of Sec. III A 3, where it was stated that the magnetic field above a certain threshold magnetic field enhances the production of the diquark condensate Δ_B, and the CSC phase can, therefore, exist up to $T \simeq 100$ MeV. In what follows, we will show that, above a certain threshold magnetic field, $\tilde{e}B_t$, the analytical results arising in a LLL approximation are comparable with the numerical results, including the contributions of all Landau levels. To do this, we will compare the analytical expression for the second-order critical lines of a transition between the χSB and the normal phase with the corresponding numerical data to determine the threshold magnetic field for the LLL approximation. A similar comparison will be, then, performed for the second-order critical line of the transition between the CSC and the normal phase.

The second-order critical surface of the transition between the χSB and the normal phase is determined explicitly in the first section of the Appendix. Here, we will present only the final results. Following the method presented in [20], in the phase space of the thermodynamical parameters $(T, \mu, \tilde{e}B)$, the second-order critical surface is determined by solving [20,21]

$$\lim_{\sigma^2\to 0}\frac{\partial\Omega_{\text{eff}}(\sigma,\Delta=0)}{\partial\sigma^2}=0. \tag{3.13}$$

Setting $n=0$ in Ω_{eff} from (2.23) and plugging the resulting expression in (3.13) leads to the second-order critical surface in the phase space of these parameters [see (A10) in the Appendix]

$$\frac{1}{4G_S}-\frac{1}{4\pi^2}\int_0^{\Lambda}dz\left(2z+\frac{3\tilde{e}B}{z}\right)F[z;T,\mu]=0, \tag{3.14}$$

with

$$F[z;T,\mu]\equiv\frac{\sinh(\beta z)}{\cosh(\beta z)+\cosh(\beta\mu)}. \tag{3.15}$$

Expanding the integral in (3.14) in the orders of $\kappa\equiv\frac{\mu}{\Lambda}$ and keeping only terms of the order $\mathcal{O}(\kappa^3)$, we arrive, after a straightforward computation, at [see also (A17) in the Appendix]

$$\begin{aligned}\mu^2(T,\tilde{e}B;\Lambda)\approx\frac{1}{\alpha}\bigg\{&-\frac{\pi^2}{G_S}+4T^2\bigg[\lambda^2-\text{Li}_2(-e^{-2\lambda})\\&+2\lambda\ln(1+e^{-2\lambda})-\frac{\pi^2}{12}\bigg]\\&+3\tilde{e}B\int_0^{\lambda}dz\frac{\tanh z}{z}\bigg\},\end{aligned} \tag{3.16}$$

where $\lambda\equiv\frac{\Lambda}{2T}$, and α is defined by

$$\begin{aligned}\alpha(T,\tilde{e}B;\Lambda)\equiv{}&(\tanh\lambda+\lambda\tanh^2\lambda-\lambda)+\frac{3\tilde{e}B}{8T^2}\frac{\tanh^2\lambda}{\lambda}\\&+\frac{3\tilde{e}B}{8T^2}\int_0^{\lambda}dz\frac{\tanh^2 z}{z^2}.\end{aligned} \tag{3.17}$$

Moreover, $\text{Li}_2(z)$ in (3.16) is the dilogarithm function defined by

$$\text{Li}_2(z)\equiv-\int_0^{z}dz\frac{\ln(1-z)}{z}. \tag{3.18}$$

To determine the second-order critical line between the χSB and the normal phase in the $T-\mu$ plane, we have to fix $\tilde{e}B$. The analytical results arising from the LLL approximation are demonstrated in Fig. 12 by red dots. Blue solid lines denote numerical results for second-order critical lines, including the contributions of all Landau levels. In Fig. 12, the analytical and the numerical results for $\tilde{e}B=0.5\ \text{GeV}^2$, approximately at the threshold, and for $\tilde{e}B=0.7\ \text{GeV}^2$, above the threshold magnetic field, are compared. The qualitative behavior of two curves coincides above the threshold magnetic field $\tilde{e}B_t\simeq 0.5\ \text{GeV}^2$, where the system is in the regime of LLL dominance.

Similarly, the second-order critical surface between the CSC and the normal phase is determined from [20,21]

$$\lim_{\Delta^2\to 0}\frac{\partial\Omega_{\text{eff}}(\sigma=0,\Delta)}{\partial\Delta^2}=0. \tag{3.19}$$

Setting $n=0$ in Ω_{eff} from (2.23) and plugging the resulting expression in (3.19), we arrive at [see (A21) in the Appendix]

$$\tilde{e}B^{-1}(T,\mu;\Lambda)=\frac{G_D}{\pi^2}\left[H\left(\frac{\Lambda+\mu}{2T}\right)+H\left(\frac{\Lambda-\mu}{2T}\right)\right], \tag{3.20}$$

where $H(z)$ is

$$H(z)\equiv\sum_{n=1}^{\infty}\frac{(-1)^{n-1}2^{2n}(2^{2n}-1)z^{2n-1}}{(2n-1)(2n)!}B_n. \tag{3.21}$$

Here, B_n are the Bernoulli's numbers. Equation (3.20) leads to a relation between the phase-space parameters $(T,\mu,\tilde{e}B)$. In Fig. 13, we have fixed $\tilde{e}B$ to be $\tilde{e}B=0.5, 0.7\ \text{GeV}^2$ and compared the analytical data of the second-order critical line (red dots), arising from (3.20) and (3.21) with the numerical data (blue solid line). For $\tilde{e}B>\tilde{e}B_t\simeq 0.5\ \text{GeV}^2$, the analytical and numerical data exactly coincide (see the plot of $\tilde{e}B=0.7\ \text{GeV}^2$ in

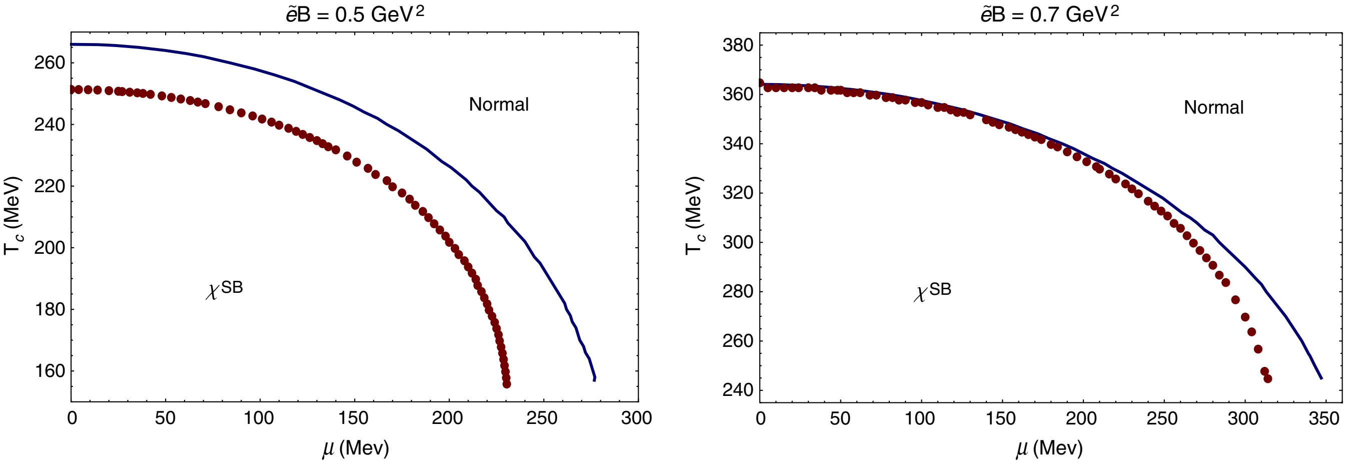

FIG. 12 (color online). The second-order critical lines of transition between the χSB and the normal phase. The red dots denote the analytical data that arise in a LLL approximation, and the blue solid line the numerical data, including the contributions of all Landau levels. For $\tilde{e}B=0.7\ \text{GeV}^2$ stronger than $\tilde{e}B_t$, the analytical and numerical data exactly coincide.

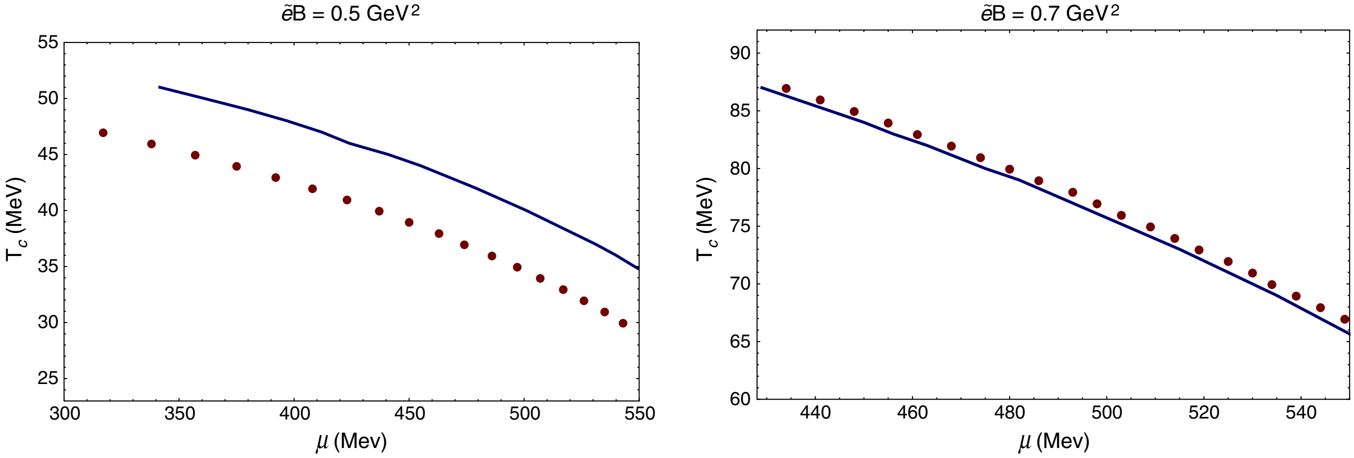

FIG. 13 (color online). The second-order critical lines of transition between the CSC and the normal phase. The red dots denote the analytical data that arise in a LLL approximation, and the blue solid line the numerical data, including the contributions of all Landau levels. For $\tilde{e}B = 0.7$ GeV^2 stronger than $\tilde{e}B_t$, the analytical and numerical data exactly coincide.

Fig. 13). We conclude, therefore, that for $\tilde{e}B > \tilde{e}B_t$, the higher Landau levels are decoupled, and the properties of the phase transitions are essentially affected by the contribution from the LLL.

2. $T - \tilde{e}B$ *phase diagram for various fixed* μ

In Fig. 14, the $T - \tilde{e}B$ phase diagram of hot 2SC quark matter is presented for various μ. Blue solid lines denote the second-order phase transitions, and the green dashed lines the first-order transitions. The critical points are denoted by C, and the tricritical points by T. The exact numerical values of the critical and tricritical points are presented in Table II.

In Figs. 14(a) and 14(b), the critical lines are plotted for $\mu = 0, 200, 250$ MeV and $\mu = 270, 280$ MeV, respectively. For relatively small values of $\mu \lesssim 270$ MeV, the transition between the χSB and the normal phase is of second order for the whole range of the magnetic field $\tilde{e}B \in [0, 0.8]$ GeV^2. When we increase the chemical potential to $\mu = 270, 280$ MeV in Fig. 14(b), the type of phase transition changes from second to first order in the regime $\tilde{e}B \in [0.1, 0.5]$ GeV^2 below the threshold magnetic field. By increasing the magnetic field and entering the regime of LLL dominance, the first-order phase transition goes over into a second-order transition (see Table II for the exact values of the critical points). The same effect has been previously observed in [21] {see Fig. 4(b) in [21] and compare it with Figs. 14(a) and 14(b) of the present paper}. In Fig. 14(c), the chemical potential is increased to $\mu = 300$ MeV. Here, a small region of the CSC phase appears in the regime $\tilde{e}B \in [0.1, 0.3]$ GeV^2, between two regions of the χSB phase. The critical points appearing in Fig. 14(a) are shifted to higher $(T, \tilde{e}B)$ (see also Table II). The small CSC "island" enlarges by increasing the chemical potential to $\mu = 310$ MeV in Fig. 14(d) and totally removing the χSB phase appearing at $\tilde{e}B \lesssim 0.15$ GeV^2 at $\mu = 325$ MeV [Fig. 14(e)]. This is expected from Figs. 2(a)–2(c), where the critical chemical potential from the transition of the χSB to the CSC phase is approximately $\mu \simeq 325$ MeV. The χSB phase appearing only for strong magnetic fields survives, but it is pushed away to the regime of LLL dominance by increasing the chemical potential to $\mu = 340$ and $\mu = 370$ MeV in Figs. 14(f) and 14(g). We notice that the transition from the χSB to the CSC phase is always of first order, whereas the type of phase transition from the χSB to the normal phase depends on the external magnetic field. This confirms our conclusion from the previous section (see Fig. 11 and the discussion in Sec. III B 1). Increasing the chemical potential to $\mu \geq 400$ MeV, the χSB region is completely removed from the interval $\tilde{e}B \in [0, 0.8]$ GeV^2, and a second-order phase transition appears between the CSC and the normal phase in Fig. 14(h). In Fig. 14(i), the second-order phase transition is plotted for $\mu = 460, 500$ MeV.[15] Above the threshold magnetic field, the critical temperature increases by increasing the magnetic field. This may open the possibility to observe the 2SC phase in future heavy-ion experiments.

Let us also emphasize that the plots in Fig. 14 are in very good agreement with plots from previous sections. As an example, let us consider Fig. 6(b), the $\tilde{e}B$ dependence of Δ_B at fixed $\mu = 460$ MeV, and compare it with the curve $\mu = 460$ MeV in Fig. 14(i). Let us, then, focus on the range of $\tilde{e}B \in [0.4, 0.6]$ GeV^2 in both figures. As it turns out from Fig. 6(b), at the low temperature $T = 20$ MeV, $\Delta_B \simeq 70$–80 MeV in the interval $\tilde{e}B \in [0.4, 0.6]$ GeV^2, while at higher temperatures $T = 60, 70$ MeV, Δ_B

---

[15] In Fig. 14(i), we have changed the scale of the plot from $T \in [0, 360]$ MeV to $T \in [35, 125]$ MeV, in order to magnify the van Alphen-de Haas oscillations that appear in the regime below the threshold magnetic field $\tilde{e}B_t \simeq 0.5$ GeV^2.

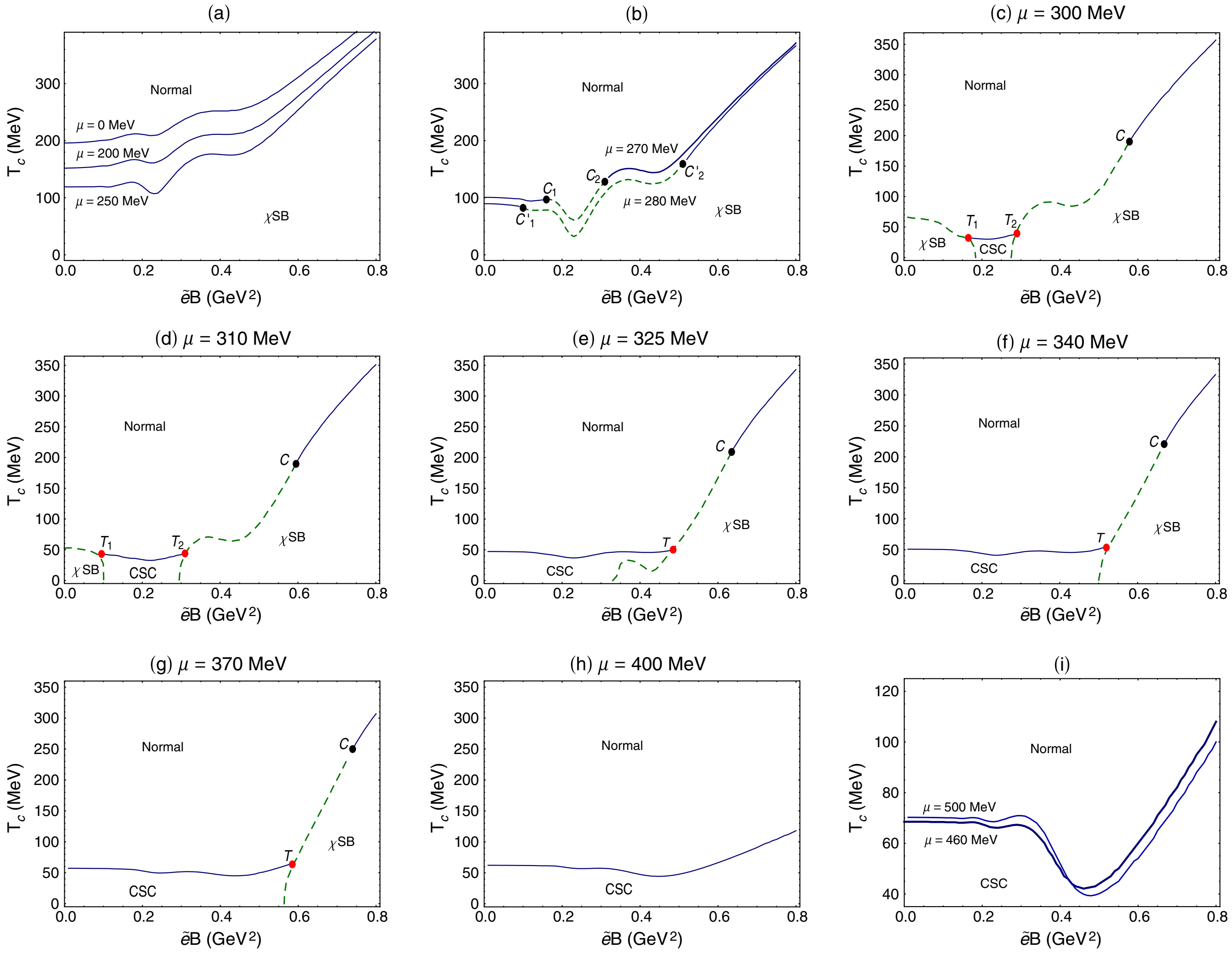

FIG. 14 (color online). The $T - \tilde{e}B$ phase diagram of hot magnetized 2SC quark matter is presented for various μ. Blue solid lines denote the second-order phase transitions, and the green dashed lines the first-order transitions. The critical points are denoted by C, and the tricritical points by T.

vanishes and, apparently, a normal phase appears in this regime of $\tilde{e}B$. The appearance of a normal phase can be checked in Fig. 14(i). For fixed $T = 20$ MeV, there is a CSC phase in the regime $\tilde{e}B \in [0.4, 0.6]$ GeV^2, while at higher temperatures $T = 60$ MeV and $T = 70$ MeV, a normal phase appears in the same regime of $\tilde{e}B$. This phenomenon is because of van Alphen-de Haas oscillations that occur in this regime of $\tilde{e}B \in [0.4, 0.6]$ GeV^2 in Fig. 6 as well as in the phase diagram of Fig. 14(i).[16] Moreover, the fact that Δ_B increases for $\tilde{e}B$ stronger than a certain threshold magnetic field $\tilde{e}B_t$ shows the important interplay between the effects of temperature and the external magnetic field on the formation of bound states, which could be

TABLE II. Critical and tricritical points in the $\tilde{e}B - T$ phase diagrams of Fig. 14, denoted by $(\tilde{e}B_{\rm cr}, T_{\rm cr})_{1,2}$ and $(\tilde{e}B_{\rm tr}, T_{\rm tr})_{1,2}$, respectively. Here, $\tilde{e}B$ is in GeV^2; T and μ are in MeV.

	$T - \tilde{e}B$ phase diagram (Fig. 14)			
μ	$(\tilde{e}B_{\rm cr}, T_{\rm cr})_1$	$(\tilde{e}B_{\rm cr}, T_{\rm cr})_2$	$(\tilde{e}B_{\rm tr}, T_{\rm tr})_1$	$(\tilde{e}B_{\rm tr}, T_{\rm tr})_2$
$\lesssim 250$	-	-	-	-
270	(0.16, 97)	(0.310, 128)	-	-
280	(0.10, 83)	(0.510, 159)	-	-
300	-	(0.578, 190)	(0.165, 32)	(0.290, 39)
310	-	(0.595, 190)	(0.095, 43)	(0.310, 44)
325	-	(0.635, 209)	-	(0.485, 50)
340	-	(0.668, 221)	-	(0.520, 54)
370	-	(0.740, 250)	-	(0.585, 64)
$\gtrsim 400$	-	-	-	-

---

[16] Similar van Alphen-de Haas oscillations occur in the "gap vs eB/μ^2 graphs" of a magnetized CFL model studied in [13,14]. In [16], where the effect of magnetic fields on the 2SC gap is studied at $T = 0$, the same oscillations occur in the same regime of $\tilde{e}B$ for $\mu = 460$ MeV {see Fig. 3(a) in [16]}.

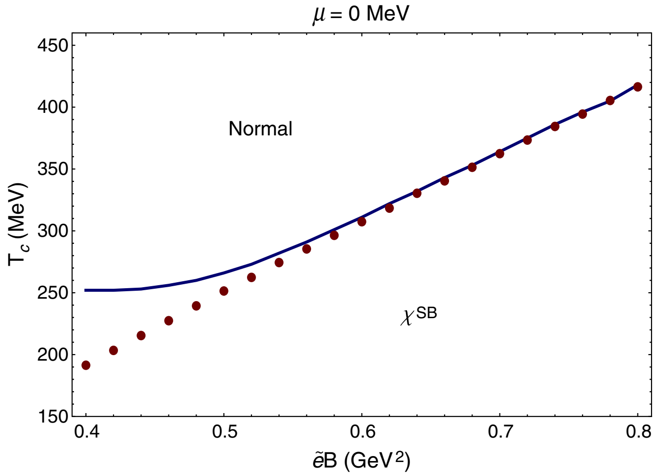

FIG. 15 (color online). The second-order critical lines of transition between the χSB and the normal phase. Red dots denote the analytical data that arise in a LLL approximation, and the blue solid line denotes the numerical data, including the contributions of all Landau levels. The threshold magnetic field is at $\tilde{e}B \simeq 0.5$ GeV^2. For $\tilde{e}B > \tilde{e}B_t$, the analytical and numerical data exactly coincide.

potentially relevant in connection with the question of accessibility of the 2SC phase in experiments. Whereas below the threshold magnetic field, by increasing the temperature, the diquark condensate is destroyed, and a normal phase is built up, the production of Δ_B is enhanced by magnetic fields stronger than $\tilde{e}B_t$ in a corresponding CSC phase. According to our previous studies in [16], we believe that, above $\tilde{e}B_t$, the system enters the LLL dominant regime, where the effect of magnetic catalysis enhances the formation of mass gaps.[17]

To show how the numerical results, including the contributions of all Landau levels, coincide with the analytical results, consisting only of the contribution of the LLL above the above-mentioned threshold magnetic field, we consider, as in the previous section, Eq. (3.14), expressing the second-order critical surface between the χSB and the normal phase. Setting, for instance, $\mu = 0$, we get, as it is shown in the first section of the Appendix, the second-order critical line in the $T - \tilde{e}B$ phase [see (A12)]:

$$\tilde{e}B(T, \mu = 0; \Lambda) = \frac{4\pi^2}{3H(\lambda)}\left\{\frac{1}{4G_S} - \frac{\Lambda^2}{4\pi^2} + \frac{T^2}{12} + \frac{T^2}{\pi^2}\left[\mathrm{Li}_2(-e^{-2\lambda}) - 2\lambda \ln(1 + e^{-2\lambda})\right]\right\}, \tag{3.22}$$

where $\lambda \equiv \Lambda/2T$. Moreover, the dilogarithm function $\mathrm{Li}_2(z)$ and $H(z)$ are defined in (3.18) and (3.21), respectively. In Fig. 15, the analytical and numerical data are compared. Red dots denote the analytical data, and the blue solid line the numerical data. Whereas, at the threshold magnetic field $\tilde{e}B_t \simeq 0.5$ GeV^2 the qualitative behavior of both data are similar, for $\tilde{e}B > \tilde{e}B_t$ the analytical and numerical data exactly coincide.

3. $\mu - \tilde{e}B$ *phase diagram for various fixed* T

In Figs. 16 and 17, the $\mu - \tilde{e}B$ phase diagram of hot magnetized 2SC quark matter is illustrated for various fixed temperatures $T = 20, \cdots 200$ MeV. Green dashed lines denote the first-order phase transitions, and blue solid lines the second-order phase transitions. The critical points are denoted by C (black bullets), and the tricritical points by T (red bullets).

Let us consider the first plot in Fig. 16, the $\mu - \tilde{e}B$ phase diagram at $T = 20$ MeV. This plot is similar to the phase diagram, which was found in [16] at $T = 0$. It includes a first-order phase transition between the χSB and the CSC phase. The latter goes over into the normal phase in a second-order phase transition.[18] This plot confirms our findings in Figs. 2(a)–2(c) and 11. At $T \simeq 50$ MeV, the CSC phase is broken into two separated islands by the normal phase, and a tricritical point (red bullet) appears at $(\tilde{e}B, \mu) = (0.490\ \mathrm{GeV}^2, 333\ \mathrm{MeV})$. The normal phase between two CSC islands appears at $\tilde{e}B \in [0.4, 0.6]$ GeV^2. This confirms our results from Fig. 7(b), where in the same regime of $\tilde{e}B$, the CSC condensate Δ_B vanishes, and a normal phase occurs. By increasing the temperature, both CSC islands shrink, so that at $T = 70$ MeV, only three separated CSC islands remain in the regime below the threshold magnetic field $\tilde{e}B \leq 0.5$ GeV^2. They are, then, totally destroyed at $T \geq 100$ MeV and in the relevant interval $\tilde{e}B \in [0, 0.8]$ GeV^2. Moreover, by increasing the temperature from $T \simeq 50$ MeV to $T \simeq 100$ MeV, the CSC island and the corresponding tricritical point that exist in the regime above the threshold magnetic field are shifted away to higher values of μ and $\tilde{e}B$ (for the exact values of the tricritical points, see Table III).

At $T \geq 100$ MeV, the $\mu - \tilde{e}B$ phase space consists only of the χSB phase and the normal phase. The critical points that appear at $T = 100$ MeV at $(0.14\ \mathrm{GeV}^2, 267.3\ \mathrm{MeV})$ are shifted to higher values of $\tilde{e}B$ and μ, as it can be seen in Fig. 17 and Table III. A high temperature suppresses the production of the chiral condensate in the regime of small magnetic fields (compare the curves in Fig. 17 in the regime $\tilde{e}B \in [0, 0.4]$ GeV^2). This effect is compensated by increasing the magnetic field to above the threshold magnetic field.

---

[17] See the explanation in Sec. I for different mechanisms being responsible for the production enhancement of meson and diquark mass gaps by strong magnetic fields.

[18] As we have explained in footnote 2, in a three-flavor NJL model at low temperature and $\mu > 500$ MeV, the CSC phase goes over into a CFL color-superconducting phase. In our model, where no CFL phase can be built, the second-order transition between the CSC and the normal phase at low temperature and $\mu > 500$ MeV is only assumed to exist. The same assumption is also made in [16].

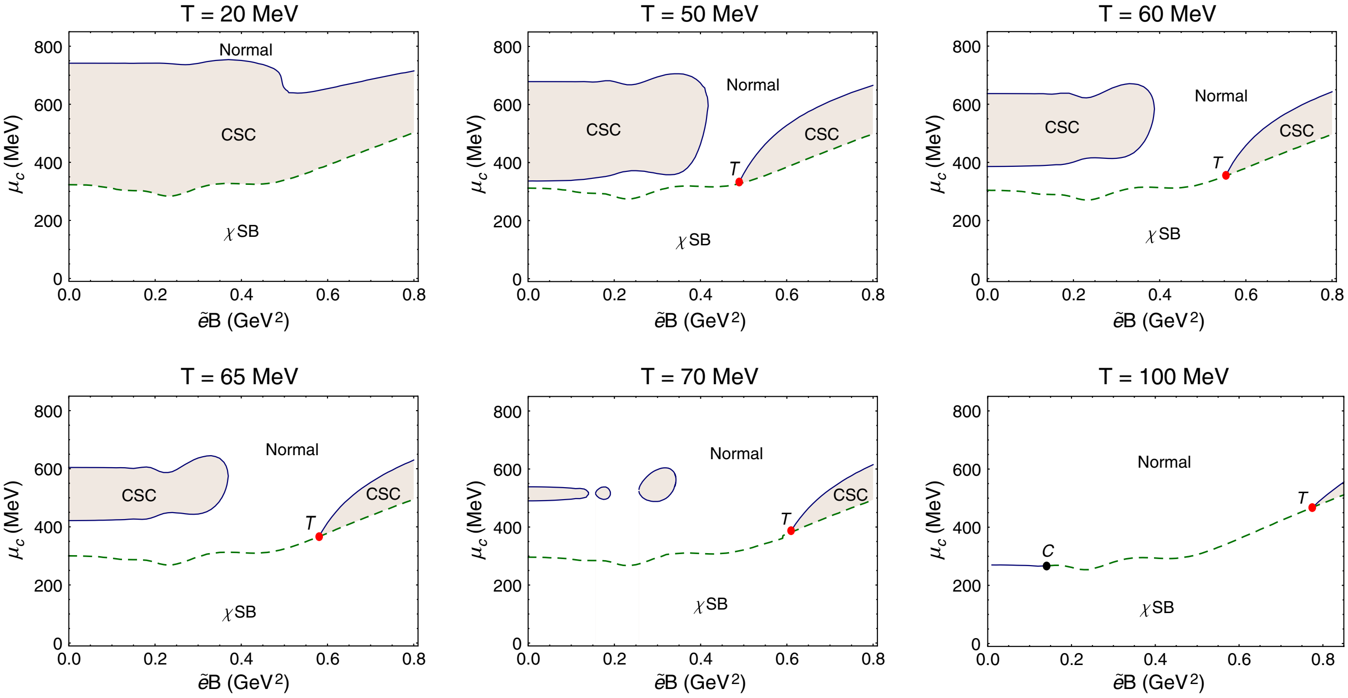

FIG. 16 (color online). The $\mu - \tilde{e}B$ phase diagram of hot magnetized 2SC quark matter is presented for various T. Blue solid lines denote second-order phase transitions, and the green dashed lines first-order transitions. The critical points are denoted by C, and the tricritical points by T. The shaded regions denote the CSC phases. A small CSC phase appears at $T = 100$ MeV on the right side of the last plot. The tricritical point (red bullet) is shifted to the regime $\tilde{e}B > 0.8$ GeV^2 (see Table III). The black bullet denotes the critical point.

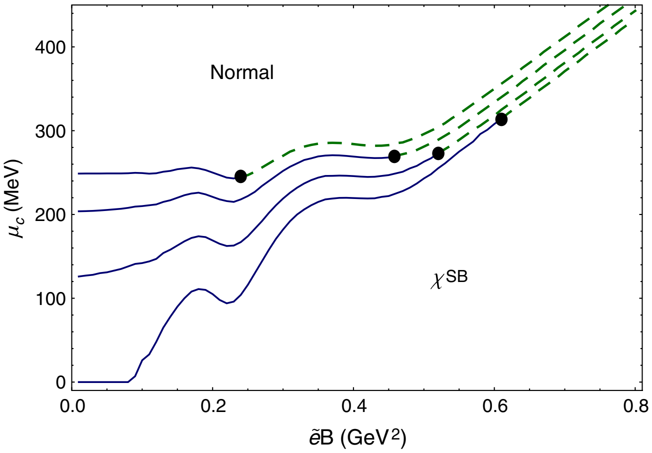

FIG. 17 (color online). The $\mu - \tilde{e}B$ phase diagram for $T = 120, 150, 180, 200$ MeV (from top to bottom).

IV. CONCLUDING REMARKS

In this paper, we have introduced a two-flavor superconducting NJL-type model, including mesons and diquarks at finite temperature T, chemical potential μ, and in the presence of a constant (rotated) magnetic field $\tilde{e}B$. We were, in particular, interested in the effect of $(T, \mu, \tilde{e}B)$ on the formation of chiral- and color-symmetry-breaking bound states and on the nature of phase transitions. One of the most important effects of the magnetic field is its competition with T and μ in the formation of bound states. This effect is demonstrated in Figs. 6 and 7. As it is illustrated in Fig. 6, although it is expected that increasing T suppresses the formation of chiral and color condensates, it turns out that this specific effect of T is minimized in the regime of a strong magnetic field for $\tilde{e}B$ larger than a certain threshold magnetic field $\tilde{e}B_t \simeq 0.5$ GeV^2. However, whereas the chiral condensate σ_B increases by

TABLE III. Critical and tricritical points in the $\tilde{e}B - \mu$ phase diagrams of Figs. 16 and 17, denoted by $(\tilde{e}B_{\rm cr}, \mu_{\rm cr})$ and $(\tilde{e}B_{\rm tr}, \mu_{\rm tr})$, respectively. Here, $\tilde{e}B$ is in GeV^2; T and μ are in MeV.

	$\mu - \tilde{e}B$ phase diagrams (Figs. 16 and 17)	
T	$(\tilde{e}B_{\rm cr}, \mu_{\rm cr})$	$(\tilde{e}B_{\rm tr}, \mu_{\rm tr})$
$\lesssim 20$	-	-
50	-	(0.490, 333)
60	-	(0.554, 356)
65	-	(0.580, 365)
70	-	(0.610, 387)
100	(0.140, 267)	(0.774, 467)
120	(0.240, 245)	-
150	(0.458, 269)	-
180	(0.520, 273)	-
200	(0.610, 314)	-

increasing $\tilde{e}B$ in the whole range of $\tilde{e}B \in [0, 0.8]$ GeV^2 [Fig. 6(a)], there are regions below $\tilde{e}B_t$ where the color condensate Δ_B vanishes [Fig. 6(b)]. The same phenomenon is also observed in Fig. 7, where, at fixed temperature and various chemical potentials, the dependence of σ_B and Δ_B on the magnetic field is plotted. Here, as in the previous case, the effect of μ in suppressing the production of the chiral and (2SC) color condensates is compensated by $\tilde{e}B$ in the regime above the threshold magnetic field.

According to our results from [16], we believe that in the regime above $\tilde{e}B_t$, the dynamics of the system are solely dominated by the lowest Landau level. In [16], a magnetized 2SC model at zero temperature is considered, and the numerical value of the threshold magnetic field is determined by comparing the analytical $\tilde{e}B$ dependence of σ_B and Δ_B, arising in a LLL approximation, with the corresponding numerical data, including the contribution of all Landau levels. According to this comparison, the threshold magnetic field at $T = 0$ turned out to be $\tilde{e}B_t \simeq 0.5$ GeV^2. In the present paper, the same model is considered at finite temperature. Comparing the analytical expression of the second-order critical line of the transitions from the χSB to the normal phase, arising from a LLL approximation, with the corresponding numerical data, including the contribution of all Landau levels in Fig. 15, we arrive at the same threshold magnetic field as in the $T = 0$ case. Note that, in [16], the color-neutrality condition was imposed on the magnetized 2SC quark matter. A comparison between the presented results in this paper, where no color neutrality is imposed, and the results from [16], shows that color neutrality, being very small [34], has no significant effect on the value of the above-mentioned threshold magnetic field.[19]

The nature of the phase transition is also affected by the external magnetic field. The most significant effect, in this regard, is illustrated in Fig. 11, where the $T - \mu$ phase space is plotted for various $\tilde{e}B$. As it is demonstrated in this figure, the phase space of the system includes three different phases. We observe that the distance between the black and red bullets, denoting the critical (C) and the tricritical (T) points, increases by increasing the strength of the external magnetic field. This implies that, by increasing $\tilde{e}B$ and keeping (T, μ) fixed, the second-order transition from the χSB phase to the normal quark matter changes into a first-order transition. This can also be observed, e.g., in Fig. 17; on each isothermal critical curve, a second-order phase transition changes into a first-order one by increasing the strength of the magnetic field. Implying external magnetic and hypermagnetic fields causes similar effects on type I QED superconductivity, as well as electroweak phase transition [3], respectively. Whereas the type of the phase transition from the χSB to the normal phase changes by increasing the strength of $\tilde{e}B$, the latter has no effect on the nature of the phase transition between the χSB and the CSC phase (first order) and between the CSC and the normal phase (second order) (see the phase diagrams in Figs. 11, 14, and 16). The only crucial effect of $\tilde{e}B$ concerning the CSC phase is the observed CSC-Normal-CSC second-order phase transition induced by strong van Alphen-de Haas oscillations in the regime $\tilde{e}B \in [0.4, 0.6]$ GeV^2 [see, e.g., Figs. 6(b) and 14(i) at fixed $T = 60$ MeV] and an increase of the tricritical temperature and chemical potential by increasing the magnetic field. The latter can be observed in Table I for $\tilde{e}B > \tilde{e}B_t \simeq 0.5$ GeV^2. This could be relevant in relation to the question addressing the accessibility of the 2SC phase in present or future heavy-ion experiments, which is recently posed in [32]. We have extended the setup of the model used in [32] by considering the effect of constant magnetic fields, which are supposed to be created in the noncentral heavy-ion collisions [28] and are estimated to be of order $\tilde{e}B \simeq 0.03$ GeV^2 at RHIC energies and $\tilde{e}B \simeq 0.3$ GeV^2 at LHC energies. These amounts of magnetic fields are, according to our observation in this extended model, far below the range of magnetic fields that could have significant effects on the CSC phase transition by partly compensating the effects of (T, μ), as described above. However, we believe that more realistic models are to be examined to find a satisfactory answer to this interesting question.

The model which is used in this paper can be extended in many ways, e.g, by considering the 2SC-CFL phase, including color neutrality. A similar computation can also be performed within a color-neutral Polyakov-NJL model. It is also intriguing to explore the effect of the axial anomaly in the same context.

ACKNOWLEDGMENTS

One of the authors (N. S.) thanks the kind support and warm hospitality of the physics department of Munich University of Technology (TUM), where the final stage of this work is done.

APPENDIX: SECOND-ORDER CRITICAL LINES IN THE LLL APPROXIMATION

In this Appendix, we will determine the main equations leading to the second-order critical lines corresponding to the transition between the χSB and the normal phase, as well as the transition between the χSB and the CSC phase, in the limit of a very strong magnetic field in the LLL approximation.

1. Transition between the χSB and the normal phase

In the phase space spanned by the intensive thermodynamical parameters $(T, \mu, \tilde{e}B)$, the second-order critical surface between the χSB and the normal phase is determined by [20,21]

---

[19] See footnote 9.

$$\lim_{\sigma^2\to 0}\frac{\partial\Omega_{\text{eff}}(\sigma,\Delta=0)}{\partial\sigma^2}=0. \tag{A1}$$

Using Ω_{eff} from (2.23) and setting $n=0$, to consider only the contribution of the lowest Landau level, we get first

$$\begin{aligned}\frac{1}{4G_S}-\frac{1}{2\sqrt{\pi}}\sum_{\kappa=\pm1}\bigg\{\iint\frac{d^3p}{(2\pi)^3}\int_0^\infty\frac{ds}{\sqrt{s}}\frac{p+\kappa\mu}{p}e^{-s(p+\kappa\mu)^2}\\ +3\tilde{e}B\int_0^\infty\frac{ds}{\sqrt{s}}\int_0^\infty\frac{dp_3}{4\pi^2}\frac{p_3+\kappa\mu}{p_3}e^{-s(p_3+\kappa\mu)^2}\bigg\}\\ \times\bigg[1+2\sum_{\ell=1}^{\infty}(-1)^\ell e^{-(\beta^2\ell^2/4s)}\bigg]=0.\end{aligned}\tag{A2}$$

Denoting the temperature-independent part of (A2) with $I_{T=0}$, and using

$$\frac{1}{2\sqrt{\pi}}\sum_{\kappa=\pm1}\int_0^\infty\frac{ds}{\sqrt{s}}\frac{x-\kappa\mu}{x}e^{-s(x-\kappa\mu)^2}=\frac{\theta(x-\mu)}{x}\tag{A3}$$

from [38], we get

$$\begin{aligned}I_{T=0}&=\frac{1}{4G_S}-\int_0^\infty\frac{pdp}{2\pi^2}\theta(p-\mu)\\&\quad-3\tilde{e}B\int_0^\infty\frac{dp_3}{4\pi^2}\frac{\theta(p_3-\mu)}{p_3}\\&=\frac{1}{4G_S}-\frac{(\Lambda^2-\mu^2)}{4\pi^2}-\frac{3\tilde{e}B}{4\pi^2}\ln\left(\frac{\Lambda}{\mu}\right).\end{aligned}\tag{A4}$$

To evaluate the momentum integration, we have introduced the ultraviolet cutoff Λ. Note that (A4) is comparable with our results from [16]. The temperature-dependent part of (A2), which is denoted by $I_{T\neq0}$, can be evaluated using

$$\begin{aligned}\sum_{\kappa=\pm1}\int_0^\infty\frac{ds}{\sqrt{s}}\frac{z-\kappa\mu}{z}e^{-s(z-\kappa\mu)^2}e^{-(\beta^2\ell^2/4s)}\\ =\frac{\sqrt{\pi}}{z}[e^{-\beta\ell|z-\mu|}\text{sgn}(z-\mu)+e^{-\beta\ell(z+\mu)}]\end{aligned}\tag{A5}$$

and is given by

$$\begin{aligned}I_{T\neq0}=\sum_{\ell=1}^{\infty}(-1)^\ell\bigg\{\int_0^\mu\frac{dz}{2\pi^2}e^{-\ell\beta\mu}\sinh(\ell\beta z)\left(\frac{3\tilde{e}B}{z}+2z\right)\\ -\int_\mu^\Lambda\frac{dz}{2\pi^2}e^{-\ell\beta z}\cosh(\ell\beta\mu)\left(\frac{3\tilde{e}B}{z}+2z\right)\bigg\},\end{aligned}\tag{A6}$$

where z is a generic integration variable replacing $p=|\mathbf{p}|$ or p_3 in the one-dimensional integrations of (A2). To perform the summation over ℓ, we use

$$\begin{aligned}\sum_{\ell=1}(-1)^\ell\sinh(\ell\beta z)e^{-\ell\beta\mu}&=\frac{1}{2}F[z;T,\mu],\\ \sum_{\ell=1}^{\infty}(-1)^\ell\cosh(\ell\beta\mu)e^{-\ell\beta z}&=\frac{1}{2}(F[z;T,\mu]-1),\end{aligned}\tag{A7}$$

where

$$F[z;T,\mu]\equiv\frac{\sinh(\beta z)}{\cosh(\beta z)+\cosh(\beta\mu)}.\tag{A8}$$

Plugging (A7) into (A6) and performing the integration over z as far as possible, the temperature-dependent part $I_{T\neq0}$ is given by

$$\begin{aligned}I_{T\neq0}=-\frac{1}{4\pi^2}\int_0^\Lambda dz\left(2z+\frac{3\tilde{e}B}{z}\right)F[z;T,\mu]\\ +\frac{(\Lambda^2-\mu^2)}{4\pi^2}+\frac{3\tilde{e}B}{4\pi^2}\ln\left(\frac{\Lambda}{\mu}\right).\end{aligned}\tag{A9}$$

The second-order critical surface of the transition between the χSB and the normal phase as a function of the phase-space variables $(T,\mu,\tilde{e}B)$ is, then, given by adding (A4) and (A9) and reads

$$\frac{1}{4G_S}-\frac{1}{4\pi^2}\int_0^\Lambda dz\left(2z+\frac{3\tilde{e}B}{z}\right)F[z;T,\mu]=0,\tag{A10}$$

where $F[z;T,\mu]$ is defined in (A8). Note that (A10) is only valid in the limit of a strong magnetic field, where a LLL approximation is justified. Choosing $\mu=0$, (A10) reads

$$\frac{1}{4G_S}=\frac{1}{4\pi^2}\int_0^\Lambda dz\left(2z+\frac{3\tilde{e}B}{z}\right)\tanh\frac{\beta z}{2}.\tag{A11}$$

This leads to the following relation between T and $\tilde{e}B$:

$$\begin{aligned}\tilde{e}B(T,\mu=0;\Lambda)=\frac{4\pi^2}{3H(\lambda)}\bigg\{\frac{1}{4G_S}-\frac{\Lambda^2}{4\pi^2}+\frac{T^2}{12}\\ +\frac{T^2}{\pi^2}\Big[\text{Li}_2(-e^{-2\lambda})-2\lambda\ln(1+e^{-2\lambda})\Big]\bigg\},\end{aligned}\tag{A12}$$

where $\lambda\equiv\Lambda/2T$,

$$H(z)\equiv\sum_{n=1}^{\infty}\frac{(-1)^{n-1}2^{2n}(2^{2n}-1)z^{2n-1}}{(2n-1)(2n)!}B_n,\tag{A13}$$

$\text{Li}_2(z)$ is the dilogarithm function defined by

$$\text{Li}_2(z)\equiv-\int_0^z dy\frac{\ln(1-y)}{y},\tag{A14}$$

and B_n are the Bernoulli's numbers. This result will be used in Sec. III B to determine the threshold magnetic field for the LLL approximation at $\mu=0$. For arbitrary values of the chemical potential, we expand (A10) in the orders of $\frac{\mu}{\Lambda}$, keep terms up to $\mathcal{O}[(\frac{\mu}{\Lambda})^3]$, and arrive at the explicit (T,μ) dependence of $\tilde{e}B$,

$$\begin{aligned}\tilde{e}B(T,\mu;\Lambda)\approx\frac{1}{3\gamma}\bigg\{-\frac{\pi^2}{G_S}+4T^2\Big[\lambda^2-\text{Li}_2(-e^{-2\lambda})\\ +2\lambda\ln(1+e^{-2\lambda})-\frac{\pi^2}{12}\Big]\\ -\mu^2(\tanh\lambda+\lambda\tanh^2\lambda-\lambda)\bigg\},\end{aligned}\tag{A15}$$

where γ is defined by

$$\gamma(T,\mu;\Lambda) \equiv \frac{\mu^2}{8T^2}\frac{\tanh^2\lambda}{\lambda} - \int_0^\lambda dz\left(\frac{\tanh z}{z} - \frac{\mu^2}{8T^2}\frac{\tanh^2 z}{z^2}\right). \tag{A16}$$

Similarly, the $(T, \tilde{e}B)$ dependence of μ is given by

$$\begin{aligned}\mu^2(T,\tilde{e}B;\Lambda) \approx \frac{1}{\alpha}\bigg\{&-\frac{\pi^2}{G_S} + 4T^2\bigg[\lambda^2 - \mathrm{Li}_2(-e^{-2\lambda})\\ &+ 2\lambda\ln(1+e^{-2\lambda}) - \frac{\pi^2}{12}\bigg]\\ &+ 3\tilde{e}B\int_0^\lambda dz\frac{\tanh z}{z}\bigg\},\end{aligned} \tag{A17}$$

where α is defined by

$$\begin{aligned}\alpha(T,\tilde{e}B;\Lambda) \equiv{}& (\tanh\lambda + \lambda\tanh^2\lambda - \lambda) + \frac{3\tilde{e}B}{8T^2}\frac{\tanh^2\lambda}{\lambda}\\ &+ \frac{3\tilde{e}B}{8T^2}\int_0^\lambda dz\frac{\tanh^2 z}{z^2}.\end{aligned} \tag{A18}$$

Relations (A17) will be evaluated numerically in Sec. III B to determine the threshold magnetic field for the LLL approximation.

2. Transition between the CSC and the normal phase

For the transition between the CSC and the normal phase, we use the equation [20,21]

$$\lim_{\Delta^2\to 0}\frac{\partial\Omega_{\text{eff}}(\sigma=0,\Delta)}{\partial\Delta^2} = 0. \tag{A19}$$

Setting $n=0$ in Ω_{eff} from (2.23) and plugging the resulting expression in (A19), we get

$$\begin{aligned}&\frac{1}{4G_D} - \frac{\tilde{e}B}{\sqrt{\pi}}\sum_{\kappa=\pm 1}\int_0^\infty\frac{ds}{\sqrt{s}}\int_0^\infty\frac{dp_3}{4\pi^2}e^{-s(p_3+\kappa\mu)^2}\\ &\quad\times\bigg[1 + 2\sum_{\ell=1}^{\infty}(-1)^\ell e^{-(\beta^2\ell^2/4s)}\bigg] = 0.\end{aligned} \tag{A20}$$

Evaluating the T-dependent and independent parts of the expression in the right-hand side of (A20) using (A3) and (A5), respectively, we arrive, after some straightforward manipulations, at the relation between the phase-space parameters $(T, \mu, \tilde{e}B)$,

$$\begin{aligned}\tilde{e}B^{-1}(T,\mu;\Lambda) &= \frac{G_D}{\pi^2}\int_0^{(\Lambda+\mu)/2T}dz\frac{\tanh z}{z}\\ &\quad+ \frac{G_D}{\pi^2}\int_0^{(\Lambda-\mu)/2T}dz\frac{\tanh z}{z}\\ &= \frac{G_D}{\pi^2}\bigg[H\left(\frac{\Lambda+\mu}{2T}\right) + H\left(\frac{\Lambda-\mu}{2T}\right)\bigg],\end{aligned} \tag{A21}$$

where $H(z)$ is defined in (A13). Fixing one of these parameters in (A21), the second-order critical lines for the transition from the CSC to the normal phase arises in the phase space of two other parameters.

[1] K. G. Klimenko, Z. Phys. C **54**, 323 (1992); V. P. Gusynin, V. A. Miransky, and I. A. Shovkovy, Phys. Rev. Lett. **73**, 3499 (1994); **76**, 1005(E) (1996).

[2] K. G. Klimenko and V. C. Zhukovsky, Phys. Lett. B **665**, 352 (2008); M. Ruggieri, arXiv:1009.2342; M. D'Elia, S. Mukherjee, and F. Sanfilippo, Phys. Rev. D **82**, 051501 (2010); P. V. Buividovich, M. N. Chernodub, E. V. Luschevskaya, and M. I. Polikarpov, Phys. Lett. B **682**, 484 (2010); N. O. Agasian and S. M. Fedorov, Phys. Lett. B **663**, 445 (2008); E. S. Fraga and A. J. Mizher, Phys. Rev. D **78**, 025016 (2008).

[3] P. Elmfors, K. Enqvist, and K. Kainulainen, Phys. Lett. B **440**, 269 (1998); V. Skalozub and M. Bordag, Int. J. Mod. Phys. A **15**, 349 (2000); A. Ayala, A. Bashir, A. Raya, and A. Sanchez, Phys. Rev. D **80**, 036005 (2009); J. Navarro, A. Sanchez, M. E. Tejeda-Yeomans, A. Ayala, and G. Piccinelli, Phys. Rev. D **82**, 123007 (2010); A. Sanchez, A. Ayala, and G. Piccinelli, Phys. Rev. D **75**, 043004 (2007); N. Sadooghi and K. Sohrabi Anaraki, Phys. Rev. D **78**, 125019 (2008).

[4] D. T. Son and A. R. Zhitnitsky, Phys. Rev. D **70**, 074018 (2004); M. A. Metlitski and A. R. Zhitnitsky, Phys. Rev. D **72**, 045011 (2005).

[5] D. T. Son and M. A. Stephanov, Phys. Rev. D **77**, 014021 (2008).

[6] I. E. Frolov, V. C. Zhukovsky, and K. G. Klimenko, Phys. Rev. D **82**, 076002 (2010).

[7] K. Fukushima, D. E. Kharzeev, and H. J. Warringa, Phys. Rev. D **78**, 074033 (2008); K. Fukushima, M. Ruggieri, and R. Gatto, Phys. Rev. D **81**, 114031 (2010); P. V. Buividovich, M. N. Chernodub, E. V. Luschevskaya, and M. I. Polikarpov, Phys. Rev. D **80**, 054503 (2009).

[8] K. Fukushima, D. E. Kharzeev, and H. J. Warringa, Nucl. Phys. **A836**, 311 (2010).

[9] J. Berges and K. Rajagopal, Nucl. Phys. **B538**, 215 (1999).

[10] M. G. Alford, J. Berges, and K. Rajagopal, Nucl. Phys. **B571**, 269 (2000); E. V. Gorbar, Phys. Rev. D **62**, 014007 (2000).

[11] E. J. Ferrer, V. de la Incera, and C. Manuel, Nucl. Phys. **B747**, 88 (2006).

[12] E. J. Ferrer and V. de la Incera, Phys. Rev. D **76**, 114012 (2007); E. J. Ferrer, V. de la Incera, and C. Manuel, Phys. Rev. Lett. **95**, 152002 (2005); E. J. Ferrer and V. de la Incera, Phys. Rev. D **76**, 045011 (2007).

[13] K. Fukushima and H. J. Warringa, Phys. Rev. Lett. **100**, 032007 (2008).

[14] J. L. Noronha and I. A. Shovkovy, Phys. Rev. D **76**, 105030 (2007).

[15] T. Mandal, P. Jaikumar, and S. Digal, arXiv:0912.1413.

[16] S. Fayazbakhsh and N. Sadooghi, Phys. Rev. D **82**, 045010 (2010).

[17] E. Elizalde, E. J. Ferrer, and V. de la Incera, Phys. Rev. D **70**, 043012 (2004); E. J. Ferrer and V. de la Incera, Int. J. Mod. Phys. A **19**, 5385 (2004).

[18] K. Farakos and N. E. Mavromatos, Phys. Rev. B **57**, 3017 (1998); V. C. Zhukovsky, K. G. Klimenko, V. V. Khudyakov, and D. Ebert, Pis'ma Zh. Eksp. Teor. Fiz. **73**, 137 (2001) [JETP Lett. **73**, 121 (2001)]; E. J. Ferrer, V. P. Gusynin, and V. de la Incera, Mod. Phys. Lett. B **16**, 107 (2002); E. V. Gorbar, V. P. Gusynin, V. A. Miransky, and I. A. Shovkovy, Phys. Rev. B **78**, 085437 (2008).

[19] K. G. Klimenko and V. C. Zhukovsky, Phys. Lett. B **665**, 352 (2008); E. Rojas, A. Ayala, A. Bashir, and A. Raya, Phys. Rev. D **77**, 093004 (2008); E. J. Ferrer and V. de la Incera, Phys. Rev. Lett. **102**, 050402 (2009); D. P. Menezes, M. Benghi Pinto, S. S. Avancini, A. Perez Martinez, and C. Providencia, Phys. Rev. C **79**, 035807 (2009); E. J. Ferrer and V. de la Incera, Nucl. Phys. B **824**, 217 (2010); N. Sadooghi, arXiv:0905.2097; A. Ayala, A. Bashir, A. Raya, and A. Sanchez, J. Phys. G **37**, 015001 (2010).

[20] S. Kanemura, H. T. Sato, and H. Tochimura, Nucl. Phys. **B517**, 567 (1998).

[21] T. Inagaki, D. Kimura, and T. Murata, Prog. Theor. Phys. **111**, 371 (2004).

[22] E. J. Ferrer, V. de la Incera, J. P. Keith, I. Portillo, and P. P. Springsteen, Phys. Rev. C **82**, 065802 (2010).

[23] D. Grasso and H. R. Rubinstein, Phys. Rep. **348**, 163 (2001); M. Giovannini and M. E. Shaposhnikov, Phys. Rev. D **62**, 103512 (2000).

[24] E. Witten, Nucl. Phys. **B249**, 557 (1985); E. M. Chudnovsky, G. B. Field, D. N. Spergel, and A. Vilenkin, Phys. Rev. D **34**, 944 (1986).

[25] A. E. Shabad and V. V. Usov, Phys. Rev. Lett. **96**, 180401 (2006).

[26] I. V. Selyuzhenkov (STAR Collaboration), Romanian reports in Physics **58**, 049 (2006).

[27] D. E. Kharzeev, L. D. McLerran, and H. J. Warringa, Nucl. Phys. A **803**, 227 (2008).

[28] V. Skokov, A. Y. Illarionov, and V. Toneev, Int. J. Mod. Phys. A **24**, 5925 (2009).

[29] W. J. de Haas and P. M. van Alphen, Proc. Acad. Sci., Amsterdam **33**, 1106 (1930); L. D. Landau and E. M. Lifshitz, *Statistical Physics* (Pergamon, New York, 1980).

[30] D. Ebert, K. G. Klimenko, M. A. Vdovichenko, and A. S. Vshivtsev, Phys. Rev. D **61**, 025005 (1999).

[31] M. Buballa, Phys. Rep. **407**, 205 (2005); M. Huang, Int. J. Mod. Phys. E **14**, 675 (2005); I. A. Shovkovy, Found. Phys. **35**, 1309 (2005); M. G. Alford, A. Schmitt, K. Rajagopal, and T. Schafer, Rev. Mod. Phys. **80**, 1455 (2008).

[32] D. B. Blaschke, F. Sandin, V. V. Skokov, and S. Typel, Acta Phys. Polon. Suppl. **3**, 741 (2010).

[33] M. Huang, P. f. Zhuang, and W. q. Chao, Phys. Rev. D **67**, 065015 (2003).

[34] M. Huang and I. Shovkovy, Nucl. Phys. **A729**, 835 (2003); I. Shovkovy and M. Huang, Phys. Lett. B **564**, 205 (2003).

[35] e.g., D. Ebert, K. G. Klimenko, and V. L. Yudichev, Phys. Rev. C **72**, 015201 (2005); D. Blaschke, D. Ebert, and K. G. Klimenko *et al.*, Phys. Rev. D **70**, 014006 (2004); D. Ebert, V. V. Khudyakov, and V. C. Zhukovsky *et al.*, Phys. Rev. D **65**, 054024 (2002).

[36] M. G. Alford, Annu. Rev. Nucl. Part. Sci. **51**, 131 (2001).

[37] R. D. Pisarski and D. H. Rischke, Phys. Rev. D **61**, 051501 (2000); A. Schmitt, Q. Wang, and D. H. Rischke, Phys. Rev. D **66**, 114010 (2002); D. Ebert, K. G. Klimenko, and H. Toki *et al.*, Prog. Theor. Phys. **106**, 835 (2001).

[38] D. Ebert, K. G. Klimenko, V. C. Zhukovsky, and A. M. Fedotov, Eur. Phys. J. C **49**, 709 (2007).